Ultrasound imaging of injections in masseter muscle without contrast agent using strain elastography and a novel B-mode spatiotemporal filter

Sanabria, Sergio J ; Ruby, Lisa ; Kuonen, Jasmine ; Dettwiler, Susanne ; Colombo, Vera ; Frauenfelder, Thomas ; Ettlin, Dominik ; Rominger, Marga B

Abstract: Botulinum toxin type A (BTX-A) injections in masseter muscle can alleviate muscle tightness and aching pain caused by idiopathic masticatory myalgia, a subform of the myofascial pain syndrome. Yet the injection procedure (number, amount) is currently empirical. In this ex vivo study, we determined the feasibility of using contrast-free ultrasound imaging to visualize the short-term injectate propagation. Ultrasound annotations of BTX-A injectate spread in N = 12 porcine masseter muscles were compared with the histopathology of the excised masseter. BTX-A presence was automatically detected in the ultrasound cine by: compensating tissue motion and deformation during injection with a novel spatiotemporal filtering (SF) algorithm, and by imaging tissue swelling strains with strain elastography (SE). BTX-A injectate introduced 6.5% (standard deviation = 5.0%) echogenicity contrast and 13.9% (standard deviation = 3.7%) tissue swelling strain. Muscle fasciae were a border for BTX-A distribution. The SF algorithm achieved significantly higher noise rejection (contrast-to-noise ratio = 4.63) than SE (2.56, $p = 0.01$), and state-of-the-art 2-D digital image correlation (1.81, $p < 0.001$) and direct image subtraction (1.29, $p < 0.001$) methods. Histopathology agreed well with ultrasound (Dice coefficient = 0.48), with deviations mainly explained by the three-dimensional inhomogeneous distribution of BTX-A. Preliminary in vivo patient results indicated that SF and SE discard artifactual BTX-A detection outside the injection region. The proposed methods contribute to objectivize ultrasound-guided injections, with additional applications, for instance, to monitor injectate spread of local anesthetics.

DOI: https://doi.org/10.1016/j.ultrasmedbio.2020.06.022

DOI: https://doi.org/10.1016/j.ultrasmedbio.2020.06.022

Ultrasound in Med. & Biol., Vol. 46, No. 10, pp. 2717–2735, 2020

0301-5629/$ - see front matter

https://doi.org/10.1016/j.ultrasmedbio.2020.06.022

● *Original Contribution*

ULTRASOUND IMAGING OF INJECTIONS IN MASSETER MUSCLE WITHOUT CONTRAST AGENT USING STRAIN ELASTOGRAPHY AND A NOVEL B-MODE SPATIOTEMPORAL FILTER

Sergio J. Sanabria,* Lisa Ruby,* Jasmine Kuonen,* Susanne Dettwiler,† Vera Colombo,‡ Thomas Frauenfelder,* Dominik Ettlin,‡ and Marga B. Rominger*

* Zurich Ultrasound Research and Translation (ZURT), Institute of Diagnostic and Interventional Radiology, University Hospital Zurich, Zurich, Switzerland; † Institute of Pathology and Molecular Pathology, University Hospital Zurich, Zurich, Switzerland; and ‡ Clinic of Masticatory Disorders, Center of Dental Medicine, University of Zurich, Zurich, Switzerland

(*Received* 21 *February* 2020; *revised* 28 *May* 2020; *in final from* 27 *June* 2020)

Abstract—Botulinum toxin type A (BTX-A) injections in masseter muscle can alleviate muscle tightness and aching pain caused by idiopathic masticatory myalgia, a subform of the myofascial pain syndrome. Yet the injection procedure (number, amount) is currently empirical. In this *ex vivo* study, we determined the feasibility of using contrast-free ultrasound imaging to visualize the short-term injectate propagation. Ultrasound annotations of BTX-A injectate spread in N = 12 porcine masseter muscles were compared with the histopathology of the excised masseter. BTX-A presence was automatically detected in the ultrasound cine by: compensating tissue motion and deformation during injection with a novel spatiotemporal filtering (SF) algorithm, and by imaging tissue swelling strains with strain elastography (SE). BTX-A injectate introduced 6.5% (standard deviation = 5.0%) echogenicity contrast and 13.9% (standard deviation = 3.7%) tissue swelling strain. Muscle fasciae were a border for BTX-A distribution. The SF algorithm achieved significantly higher noise rejection (contrast-to-noise ratio = 4.63) than SE (2.56, $p = 0.01$), and state-of-the-art 2-D digital image correlation (1.81, $p < 0.001$) and direct image subtraction (1.29, $p < 0.001$) methods. Histopathology agreed well with ultrasound (Dice coefficient = 0.48), with deviations mainly explained by the three-dimensional inhomogeneous distribution of BTX-A. Preliminary *in vivo* patient results indicated that SF and SE discard artifactual BTX-A detection outside the injection region. The proposed methods contribute to objectivize ultrasound-guided injections, with additional applications, for instance, to monitor injectate spread of local anesthetics. (E-mail: sanse@stanford.edu) © 2020 The Author(s). Published by Elsevier Inc. on behalf of World Federation for Ultrasound in Medicine & Biology. This is an open access article under the CC BY-NC-ND license. (http://creativecommons.org/licenses/by-nc-nd/4.0/).

Key Words: **Ultrasound-guided injections, Myofascial pain, Botulinum toxin type A, Motion compensation, Spatiotemporal filtering, Strain elastography, Histopathology.**

INTRODUCTION

Masticatory muscle pain is the primary cause for chronic non-odontogenic orofacial pain, affecting about 12%–14% of the adult population, and is related to common mental states (depression, anxiety, mood and stress-related disorders) (Wieckiewicz et al. 2017). Clinical symptoms of idiopathic masticatory myalgia (IMM) include muscle tightness, aching pain and/or muscular tenderness (Solberg 1986; Clark 2008; Awan 2017). Botulinum toxin type A (BTX-A) is synthesized by the bacterium *Clostridium botulinum* and works through blockade of the release of acetylcholine into the synaptic cleft and inhibition of the release of neurotransmitters at sensory nerve endings (Figgit and Noble 2002). Several randomly allocated placebo-controlled trials have indicated the potential of BTX-A in improving symptoms in IMM (von Lindern et al. 2003; Guarda-Nardini et al. 2008; Kurtoglu et al. 2008). Electromyographically, BTX-A injections resulted in a decrease in action potential (Kurtoglu et al. 2008). However, the procedure (number of injections, amount of injectate) is empirical, and distribution patterns of the substance are currently unknown (Zhou and Wang 2014). BTX-A injections are applied in many additional clinical contexts, such as non-physiologic muscle activity (spasticity,

Address correspondence to: Sergio J. Sanabria, Stanford Ultrasound Research Group, Department of Radiology, Stanford Medicine, 3155 Porter Drive, MC 5483, Palo Alto, CA 94303, USA. E-mail: sanse@stanford.edu

tremors, dystonia), neurosecretory dysfunction (sialorrhea) and pain conditions, as well as esthetic medicine (Alter and Karp 2018).

Several guidance approaches have been proposed to monitor BTX-A injections. Palpation requires no technology, but cannot distinguish muscle depth or anatomic variations, and is applicable only for superficial muscles. Electromyography is useful in identifying muscle targets and motor points based on their activity, and is useful in patients with focal dystonia, but it does not provide spatially resolved imaging of muscle and surrounding tissue structures. Similarly, electrical stimulation (E-Stim) is applied in upper motor neuron syndromes but is associated with discomfort to the patient. Imaging techniques such as fluoroscopy, computed tomography and magnetic resonance can help to better identify some muscle anatomic structures; however, they either require ionizing radiation or are costly (Alter and Karp 2018).

Ultrasound (US) is a radiation-free, tolerable and cost-efficient modality, which is widely available for tissue and pathology diagnostics. US-guided injections are increasingly used to guide musculoskeletal interventions, allowing for continuous real-time visualization of needle and target muscles, as well as structures to be protected (Bruyn and Schmidt 2009; Epis and Bruschi 2014; Daniels et al. 2018). Clinical outcomes of US-guided BTX-A injections have been reported, for example, for sialorrhea (Dogu et al. 2004), muscle spasticity (Sconfienza et al. 2009) and cervical dystonia (Hong et al. 2012). US guidance increases safety and reduces adverse effects. On the other hand, training is required for sonographic examination, and the outcome is operator dependent. In general, US-guided injections typically rely on visualization of the echogenic needle tip before injection and correct alignment with respect to target tissue structures. Injectate spread is currently qualitatively identified by comparison of multiple frames in the US cine, where small image contrast variations and tissue movement and deformation during the injection process are visually identified (Marhofer et al. 2005; Bloc et al. 2007; Tran et al. 2009; McCartney et al. 2010; Andersen et al. 2012). Recently, contrast-enhanced US (CEUS) has been proposed to enhance the contrast of the injectate in US images (Sasaki et al. 2017). However, CEUS complicates the injection workflow, is off-label, may affect the injection outcome or may have additional complications for the patient, all of which need to be carefully verified for each clinical case.

The goal of this work was to improve the visualization of injectate by using conventional US images (B-mode), without the need for a contrast agent. First, we acquired a cine of B-mode frames during the injection process. Next, we used image registration to compensate for tissue deformation. We exploited the temporal characteristics of the injection process. This allows filtering out tissue structures from the images and highlighting small tissue echogenicity and strain variations, which are caused by the presence of injectate. In the context of this work, the term *deformation compensation* is methodologically equivalent to motion compensation, where motion specifically refers to tissue displacements caused by physiologic movement, and *deformation* is a more generic term that also includes tissue displacements causes by tissue swelling. US imaging of BTX-A is finally compared with histopathological assessment of excised tissue specimens as the reference standard.

METHODS

Experiments

Test patients and injectates. Masseter phantom with contrast agent. In the setup phase, we examined injections on fresh loin porcine muscle from the local slaughterhouse, which was placed in a plastic box and examined within 12 h after explantation. A 1-mL NaCl 0.9% solution (B. Braun, Bethlehem, PA, USA) was mixed with US contrast agent (SonoVue 8 μl/mL, Bracco, Milan, Italy). The masseter phantom was injected with 1 mL of the compound.

Ex vivo *porcine masseter without contrast agent.* Six heads of adult domestic pigs (*Sus scrofa domesticus*) (M1−M6) with 12 intact masseter muscles (right [R]/left [L]) were obtained from the local slaughterhouse under supervision of their veterinary department within 6 h after butchering. The cutis, subcutis and superficial muscle layers were dissected to reveal the masseter in its entirety. BTX-A (Xeomin, 150 kD, 50 LD50, Merz Pharma, Frankfurt am Main, Germany) was diluted in 1 mL NaCl 0.9% (B. Braun). 0.5 mL of BTX-A and 0.5 mL indigo carmine (4 mg/mL, Amino AG, Gebenstorf, Switzerland) were mixed (1:1 ratio). No US contrast agent was administered. Eight masseter muscles (M1−M4) were injected with 0.25 mL of the compound, whereas 0.5 mL was injected in the remaining four muscles (M5 and M6).

In vivo *volunteer.* A 40-y-old female patient diagnosed with IMM was scheduled for BTX-A injection. She had no prior exposure to this medication. Ultrasound was approved by the Ethics Committee of the State of Zurich (KEK-ZH No 2019-01396), and HIPAA-compliant informed consent was obtained from the patient. The BTX-A injectate consisted of 1.25 mL NaCl containing 12.5 units of BTX-A. This was slowly infiltrated into the anterior and posterior portions of each masseter muscle.

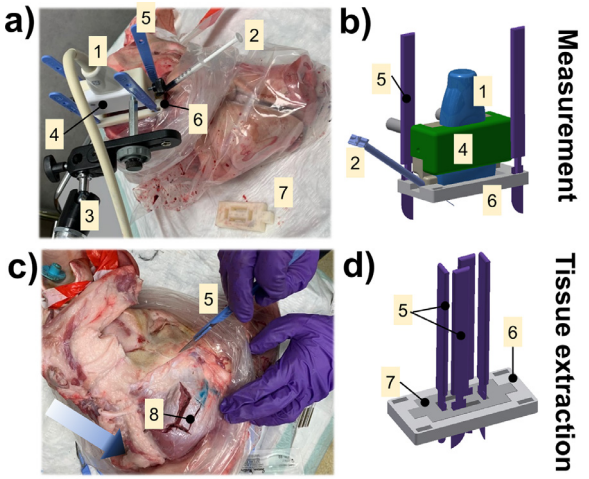

Fig. 1. Experimental setup. (a) Ultrasound measurement (US): Probe (1) and syringe (2) are positioned coplanar and fixed with four scalpels (5) to porcine masseter. (b) Computer-aided design schematic of 3-D-printed probe holder (4) and measurement frame (6). (c) Tissue extraction: The US probe is removed and a 3-D-printed extraction frame (7) is inserted into (6) to reproducibly cut out masseter tissue (8) with a scalpel (5). (d) Computer-aided design schematic of tissue extraction frame.

Each injection was aimed at depositing the injectate into the deepest third of the muscle.

US examination. For phantom and *ex vivo* experiments, US examinations were performed using a 9 L-D linear probe (GE Healthcare, Chicago, IL, USA) (bandwidth of 2-9 MHz, 192 elements, footprint 44 mm, array pitch 229 μm) and a GE Logiq E9 US system (Fig. 1). The probe was fixed in a direction perpendicular to the muscle fibers using a 3-D-printed transducer holder and a positioning arm (244 N, Manfrotto, Cassola, Italy). The holder included a guide tunnel for the syringe on the side (1 mm diameter), which ensured that the syringe was placed coplanar to the ultrasound probe with 35° inclination and reproducible insertion depth (Fig. 2a). The needle (25 G × 1 in., 0.50 × 25 mm BL/LB, Gr 17/23) was placed on a 25G 1-mL syringe (Primo Luer Tuberculin 1 mL H82246-1, Codan Medical ApS, Denmark). The needle tip was located at 13-mm axial depth, 13-mm lateral position and at half of the transducer elevational plane (5.5 mm) and was tilted 35° with respect to the lateral axis of the transducer. To analyze the variability of ultrasound images, 10 s of the ultrasound cine was recorded before injection. Afterward, the BTX-A−indigo carmine compound was injected (0.25 mL/3 s). The recording was stopped after 60 s. US frame cine was exported as an offline video in MPG format

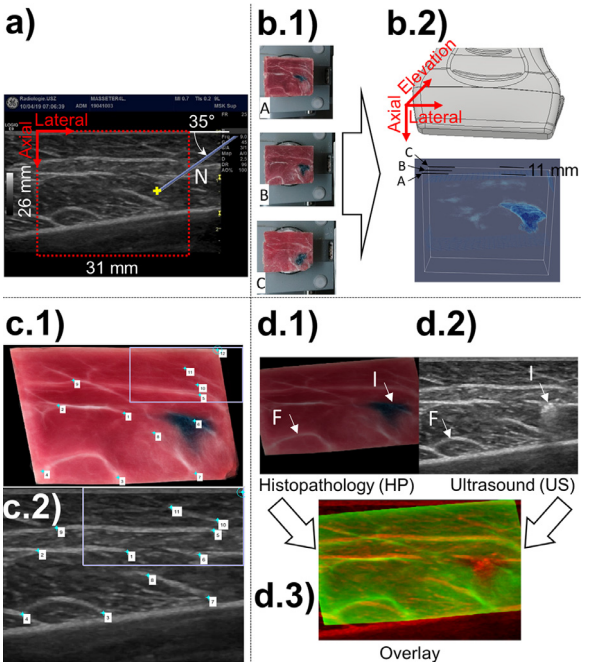

Fig. 2. Co-registration of ultrasound (US) and histopathology (HP). (a) US B-mode image. Nominal needle (N) and injection point (*yellow cross*) positions are marked, together with extracted HP region (*dashed red rectangle*). (b.1) Optic HP images after successive cryostat cuts (A, B, C) were rendered into a three-dimensional (3-D) volume (b.2) over the US measurement region. (c) Manual identification of tissue landmarks (1−12) in HP (c.1) and US (c.2) images. (c.1) is an average of the HP volume (b.2) over US slice thickness (elevation). (d) Registration of HP (d.1) and US image (d.2) and overlaid visualization (d.3). A consistent overlap between US and HP is observed for muscle fascia (F) and BTX-A injection region (I).

(Fig. 2a). The recorded frame rate was 25 frames/s, resulting in 1500 frames/cine.

For the *in vivo* injection, a hockey stick probe (GE L8-18 i-D) intra-operative US transducer (bandwidth 5−9 MHz, footprint 25 mm) was placed over the thickest portion of the masseter muscle. The transducer axis was aligned with the axis of the mandibular body. In this case, the needle was inserted at a 45° angle to the longitudinal axis of the US head so that the needle tip reached the deep muscle portion in the anterior and posterior thirds of the muscle. To avoid discomfort for the patient, the injection was performed immediately (without the 10-s waiting time) after the needle reached the target stable position. The transducer was attached to the holder probe during the measurement.

Histopathological assessment. Three-dimensional-printed frames were adapted to the transducer holder to ensure the extraction of *ex vivo* tissue at the measured US plane. During US data acquisition, the US probe was fitted into a measurement frame (Fig. 1a, 1b). The frame (6) had

slits at the edges, where disposable stainless-steel scalpels (size 22, model 0508, Swann-Morton, Sheffield, UK) were inserted, allowing fixation to the porcine masseter tissue. After US measurement, the frame (6) remained attached to the masseter and the US probe was removed. Then, a second 3-D-printed tissue extraction frame (7) was inserted into the measurement frame (6) (Fig. 1c, 1d). The tissue extraction frame incorporated additional slits, which allowed precise cutting and extraction of the masseter tissue (8) at the region of interest. The extracted tissue sample size was 26 mm (axial) × 31 mm (lateral) × 11 mm (elevational), which fitted exactly into the histopathological embedding cassette (Macrosette M512, Simport Scientific, Saint-Mathieu-de-Beloeil, Canada). The tissue sample was extracted from the tissue surface up to depth of 26 mm; it was laterally centered with respect to the 44-mm field of view of the 9 L-D US probe (6.5 mm cropped on each side) and covered the full US probe elevation range (11 mm). With respect to the extracted tissue sample, the needle tip was located at 50% axial, 20% lateral and 50% elevation position.

After extraction (<15 min), the masseter tissue was immediately placed on ice and deep frozen within 60 min (Snapfrost, Excilone, Elancourt, France). The extracted tissue sample was cut into 20-μm-thick slices with a Cryostat (Hyrax C60, Carl Zeiss MicroImaging GmbH, Jena, Germany); 20 slices/sample were extracted with 500-μm steps along the transducer elevation direction. For each histopathological slice, optic images were acquired with a digital camera (PowerShot SX730 HS, Canon Inc., Tokyo, Japan) (Fig. 2b.1).

Registration of histopathology and ultrasound images. The 20 acquired histopathological slices images were co-registered with each other to obtain a 3-D optic stack (Fig. 2b.2). The plugin "Register Virtual Stack Slices" (Arganda-Carreras et al. 2006) from FiJi/ImageJ (1.51 n) was used (Schindelin et al. 2012) (for further details, see the Appendix). An average image of the 3-D stack was calculated to obtain a mean optic representation of the 2-D region of interest measured by the US probe (Fig. 2c.1). The calculated mean optic images were registered with their corresponding US images before the start of the injection process. Common features in both optic and ultrasonic images were manually extracted by one examiner (J.K.) using the Control Point Selection (cpselect) of MATLAB (2016 b, The MathWorks Inc., Natick, MA, USA). Ten to twenty feature points were extracted from each image at fascia corners or branching points (Fig. 2c.2). A projective transformation was fitted to the control points to align the optic and US images (Fig. 2d).

Manual annotation of injectate extension. BTX-A injectate extension was annotated independently by two examiners (L.R., J.K.) First, each sonographer performed an annotation of the injectate spread based on visual observation of only the initial B-mode frame (before injection) and the last acquired B-mode frame (50 s after injection). Second, each sonographer performed a second annotation based on the visual observation of the full recorded US frame cine. The needle tip position was also annotated from observation of the US cine. A consensus annotation was obtained as the commonly annotated pixels by both readers. Each reader additionally evaluated the level of difficulty for the video-based and image-based injectate annotations using a Likert score (1 = very easy, 2 = easy, 3 = neutral, 4 = difficult, 5 = very difficult). The BTX-A injectate extension was annotated in the optical histopathology images (before registration with US) by one examiner (S.J.S). The annotations of US and optic images were performed in a blinded way.

Automatic quantification of injectate spread based on tissue deformation compensation and spatiotemporal filtering

US tracking of injectates in muscles reveals characteristic spatiotemporal features, which are utilized as assumptions to build automatic quantification of injectate spread:

1. The injection process induces local swelling of adjacent tissue during the expansion of the injectate, which is assumed to be characterized by a heterogeneous deformation pattern.
2. Musculoskeletal tissue contains hyper-echogenic muscle fasciae, which are characterized by a higher echogenicity compared to muscle fascicles and injectate, and thus show strongly dominant contrast features in the ultrasound images. Therefore, tissue deformation compensation is expected to be affected by strong bias.
3. Correlation between ultrasound frames is reduced with increasing time separation between compared frames. One reason for this lies in out-of-plane movements of the hand-held US probe, which significantly affect the ultrasound echogenicity patterns.
4. Local tissue deformations contain relevant information on the injectate presence.

First, we quantify tissue echogenicity changes caused by injectate presence. Under assumption 1, we compare deformation compensation based on frame Direct Subtraction (DS) with frame subtraction after deformation compensation using a state-of-the-art algorithm (Two-Dimensional Digital Image correlation [2-D-DIC]) (O'Donnell et al. 1994; Pan et al. 2009). Next,

we introduce a novel Spatiotemporal Filtering (SF) algorithm, which exploits assumptions 2 and 3. Finally, we apply Strain Elastography (SE) to visualize injectate-induced tissue swelling (assumption 4).

Next, the methodological workflow for each of the algorithms is outlined. Implementation details for each computational step and examples are provided in the Appendix.

Direct Subtraction. Echogenicity contrast caused by injectate is visualized by subtracting the acquired B-mode frames $F_2, F_3, F_4, \ldots$ with respect to a reference frame F_1 acquired immediately before the start of the US injection process $F_2-F_1, F_3-F_1, F_4-F_1, \ldots$ (Fig. 3a).

2-D Digital Image Correlation. In a first step (Fig. 3b.1), the 2-D-DIC algorithm estimates the local deformation fields $\mathbf{u}_{2,1}, \mathbf{u}_{3,1}, \mathbf{u}_{4,1}, \ldots$ between the injection frames $F_2, F_3, F_4, \ldots$ and the reference frame F_1. For this purpose, a deformation tracking processing block DT^{ij} estimates the local deformation fields at each axial i and lateral j pixel of the image. Deformation tracking is based on finding the best local match for pixel templates in the reference and injection frames by maximizing a correlation function (see calculation details in the Appendix). At each pixel, the axial $u(i, j)$ and v(i, j) lateral displacement distributions are summarized in a deformation vector field $\mathbf{u}_{b,a} = [u(i,j), v(i,j)]_{b,a}$, where deformation in frame b is calculated with respect to a reference frame a.

In a second step (Fig. 3b.2), an interpolation block I^{ij} uses the calculated deformation fields $\mathbf{u}_{2,1}, \mathbf{u}_{3,1}, \mathbf{u}_{4,1} \ldots$ to compensate deformation and realign the acquired B-mode frames $F_2, F_3, F_4 \ldots$ with respect to F_1. The interpolation block achieves subpixel accuracy by performing a gray-scale fit using B-mode values at neighboring pixels (see Appendix for details). The deformation-corrected frames are written as $F_{2,1}, F_{3,1}, F_{4,1} \ldots$.

In a third step (Fig. 3b.3), the deformation-corrected frames $F_{2,1}, F_{3,1}, F_{4,1} \ldots$ are subtracted with respect to F_1, providing echogenicity contrast $F_{2,1}-F_1, F_{3,1}-F_1, F_{4,1}-F_1, \ldots$.

Spatiotemporal Filtering. Spatiotemporal Filtering exploits the temporal statistics of the BTX-A injection process to improve injectate delineation. Both the deformation calculation and frame subtraction steps in 2-D-DIC (Fig. 3b) are modified to accommodate spatiotemporal filters. Conceptually, SF splits the deformation and echogenicity calculation substeps into differential steps between successive frames. The splitting allows application of spatial and temporal filters to filter out

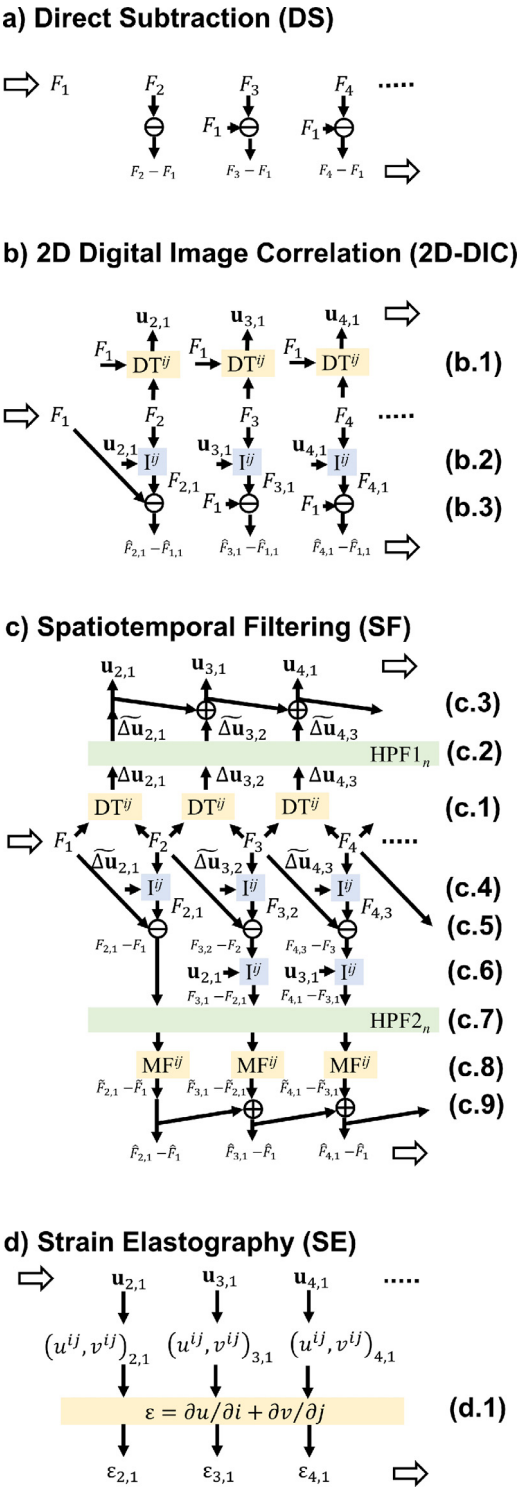

Fig. 3. Automatic algorithms for injection spread quantification. (a) Direct subtraction (DS) and (b) 2-D Digital Image Correlation (2-D-DIC) are state-of-the-art algorithms. (c) Spatiotemporal Filtering (SF) (c) and Strain Elastography (SE) are two proposed solutions, which exploit the dynamics of injection spread. DS, 2-D-DIC, and SF quantify echogenicity contrast, while SE measures tissue swelling strains.

hyper-echogenic tissue patterns and to highlight the dynamics of the injection process.

In a first step (Fig. 3c.1), deformation tracking DT^{ij} is calculated between adjacent frame pairs, that is, between frame F_2 and reference frame F_1, between frame F_3 and reference frame F_2, and so on successively. This results in differential tissue displacement fields $\Delta\mathbf{u}_{2,1}, \Delta\mathbf{u}_{3,2}, \Delta\mathbf{u}_{4,3}, \ldots$. At a sufficiently high frame rate (here 25 frames/s), variations of the imaging scene between two successive frames, for instance, because of out-of-plane probe movement, can be neglected. Therefore, deformation tracking with adjacent frame pairs provides high-quality tissue displacement estimates for all frames, characterized by larger correlation maxima. In a second step (Fig. 3c.2), a high-pass filter HPF_n along the temporal axis n is used to minimize bias patterns while preserving the injection deformation. This allows filtering out of deformation bias caused by hyper-echogenic tissue structures. Deformation bias is present as a quasi-static deformation component in all calculation steps, whereas physical deformation caused by injection occurs dynamically with varying patterns in time. In a third step (Fig. 3c.3), the filtered differential tissue displacement fields $\Delta\mathbf{u}_{2,1}, \Delta\mathbf{u}_{3,2}, \Delta\mathbf{u}_{4,3}, \ldots$, are then accumulated with respect to the reference frame F_1, resulting in cumulative displacements $\mathbf{u}_{2,1}, \mathbf{u}_{3,1}, \mathbf{u}_{4,1}, \ldots$. Accumulation of differential displacements minimizes correlation loss over time, which is present in 2-D-DIC, for instance, because of gradual out-of-plane probe drifts.

In a fourth step (Fig. 3c.4), the interpolation block I^{ij} is used with the differential tissue displacements $\Delta\mathbf{u}_{2,1}, \Delta\mathbf{u}_{3,2}, \Delta\mathbf{u}_{4,3}, \ldots$ to realign each of the acquired B-mode frames $F_2, F_3, F_4, \ldots$, with respect to their preceding frames $F_1, F_2, F_3, \ldots$, resulting in the deformation-corrected frames $F_{2,1}, F_{3,2}, F_{4,3}, \ldots$. In a fifth step (Fig. 3c.5), differential echogenicity contrast is calculated between adjacent frames pairs $F_{2,1}-F_1, F_{3,2}-F_2, F_{4,3}-F_3, \ldots$. In a sixth step (Fig. 3c.6), the interpolation block I^{ij} is used again to re-align all differential contrast images $F_{2,1}-F_1, F_{3,2}-F_2, F_{4,3}-F_3, \ldots$, with respect to the reference frame F_1. For this purpose, the cumulative displacements $\mathbf{u}_{2,1}, \mathbf{u}_{3,1}, \mathbf{u}_{4,1}, \ldots$, calculated in Figure 3c.3 are used. The resulting aligned frames are written as $F_{2,1}-F_1, F_{3,1}-F_{2,1}, F_{4,1}-F_{3,1}, \ldots$. Splitting the interpolation into two steps (Fig. 3c.4, 3c.6) allows using high-quality tissue displacement fields for differential echogenicity contrast calculation (Fig. 3c.5), where hyper-echogenic tissue structures are filtered out.

Next (Fig. 3c.7), a temporal high-pass filter HPF_n along the temporal axis n is applied to the differential contrast to further minimize the static bias patterns and to highlight the dynamic injection echogenicity variations. Additionally (Fig. 3c.8), a spatial median filter MF^{ij} is added to each frame to reduce speckle noise in the differential contrast images caused by random subpixel uncertainties in the image registration process (variance), together with a thresholding operation to separate noise from the dynamic injectate component. Finally (Fig. 3c.9), the filtered differential contrast images $\tilde{F}_{2,1}-\tilde{F}_1, \tilde{F}_{3,1}-\tilde{F}_{2,1}, \tilde{F}_{4,1}-\tilde{F}_{3,1}, \ldots$, are added to calculate the cumulative echogenicity contrast with respect to the reference frame $\tilde{F}_1$. The resulting image cine $\tilde{F}_{2,1}-\tilde{F}_1, \tilde{F}_{3,1}-\tilde{F}_1, \tilde{F}_{4,1}-\tilde{F}_1, \ldots$, provides echogenicity contrast with respect to the first frame, where SF has been used to highlight the injectate presence.

Strain Elastography. The calculated deformation fields $\mathbf{u}_{2,1}, \mathbf{u}_{3,1}, \mathbf{u}_{4,1}, \ldots$, in Figure 3c.3 are further processed to quantify tissue swelling strains during the injection process (Fig. 3d). Each 2-D vector deformation frame $\mathbf{u}_{n,1}(i, j)$, acquired at time instant n, consists of an axial $u(i, j)$ and a lateral $v(i, j)$ deformation component for each axial i and lateral j pixel of the image. Axial strain $\varepsilon_u = \partial u/\partial i$ and lateral strain $\varepsilon_v = \partial v/\partial j$ are respectively defined as the derivatives of the displacement fields, and are added to compute swelling strain $\varepsilon = \varepsilon_u + \varepsilon_v$ (Fig. 3d.1). Strain calculation filters out physiologic tissue movement and highlights local tissue deformations caused by the presence of the injectate. While deformation polarity is accounted for in the image registration (details in Appendix), SE images were visualized in absolute strain values to highlight the overall extent of the region affected by the injection.

Implementation details and chosen parameters for the computation blocks DT^{ij}, I^{ij}, HPF_n, MF^{ij}, ε are provided in the Appendix. The same parameters were used for all experiments (masseter phantom, *ex vivo* porcine masseter and *in vivo* tests). All algorithms and data evaluations were implemented in Matlab® (2018b, The MathWorks Inc.).

Quantitative evaluation metrics and statistics

The algorithms DS, 2-D-DIC and SF automatically quantify injectate echogenicity contrast (%) and SE swelling strain (%). The temporal median of each video (US cine) was calculated to summarize the injection process into a single frame, which was then compared with manual US and histopathological annotations. Contrast-to-noise ratio (CNR) (Varghese and Ophir 1998) was used to benchmark the automatic BTX-A quantification algorithms

$$\mathrm{CNR} = 100\left|\mu^*_{\mathrm{inj}} - \mu^*_{\mathrm{bg}}\right| / \sigma^*_{\mathrm{bg}} \quad (1)$$

where μ^*_{inj}, μ^*_{bg} are the average contrast in the injectate and the background regions (without injectate), and σ^*_{bg} is the standard deviation of the contrast in the background regions. CNR provides a measurement of the algorithm's capacity to discriminate injectate from normal tissue.

The BTX-A region in DS, 2-D-DIC, SE and SF was segmented with an Otsu threshold (Otsu 1979). BTX-A presence agreement between US images (manual annotations or automatic quantification) and histopathological images was evaluated in terms of the Dice coefficient (Varghese and Ophir 1998):

$$\text{Dice} = 2\left|c^*_{inj} \cap c_{inj}\right| / \left(\left|c^*_{inj}\right| \cup \left|c_{inj}\right|\right) \quad (2)$$

where c_{inj}, c^*_{inj} are the segmented injectate regions for reference and test images, respectively. The Dice coefficient ranges from 0 (no overlap between images) to 1 (perfect overlap). Injectate spread surface (mm^2) was also measured from segmentations.

Needle tip position (mm) was automatically segmented by calculating temporal contrast profiles over the segmented injectate masks. The injection start instant was tracked by identifying the rise of contrast at 25% threshold. The needle tip position was estimated as the centroid of the segmented injectate region, which was calculated at the injection start instant.

For statistics, median values are provided, together with 95% confidence intervals (CIs). Performance differences between metrics were evaluated with a paired sample *t*-test. A p value <0.05 was regarded as indicating statistical significance. To verify the *t*-test normality assumption, normal probability plots were qualitatively assessed for each evaluated metric. Furthermore, a Shapiro–Wilk test of normality was performed (Razali and Wah 2011).

RESULTS

Masseter phantom with contrast agent

Selected US cine frames during injection, visualized with both B-mode and quantitative algorithms, are plotted in Figure 4a. The algorithms DS, 2-D-DIC, and SF quantify injectate echogenicity contrast (%) and SE swelling strain (%). The NaCl solution with contrast agent in Figure 4a had high echogenicity contrast with respect to tissue background (20% of full gray scale), which allowed direct observation of the injectate (I) from time $t = 10.2$ s onward based on single B-mode frames. Acoustic shadowing artifacts (A) were observed below the injectate region. Image registration with 2-D-DIC (CNR = 3.0) revealed only a minor improvement in injectate (I) delineation and reduction of noise in the background region with respect to DS (CNR = 2.9). SF significantly increased CNR (6.6), reducing noise in the background region while preserving the injectate contrast distribution over time. Swelling strains up to 11% were measured with SE (CNR = 3.4), with spatial correspondence with the BTX-A injectate region. SE artifacts were observed in the hypo-echogenic region below the bone (B), where the US signal vanished.

Temporal profiles (Fig. 4b) illustrate the mean values as a function of time for DS, 2-D-DIC, SF and SE over annotated injectate (inj) and background (bk) regions. Temporal profiles (Fig. 4b) over the background (bk) region (Fig. 4b) exhibit an increase in background noise from $t = 10$ s (reference frame) up to ± 5 s time separation. Before injection ($t = 0$ s), DS, 2-D-DIC and SF revealed respectively 4.6%, 4.0% and 0.23% contrast in the background region, while SE revealed 1.5% contrast noise. After injection, noise increased because of the presence of acoustic shadowing (A). DS, 2-D-DIC, SF and SE revealed 7.1%, 5.3%, 2.9% and 3.5% contrast in the background region, respectively.

Ex vivo *porcine masseter without contrast agent*

The BTX-A injectate without contrast agent in Figure 5 exhibited low echogenicity contrast (4.4%), which did not allow visualization based on single B-mode frames. A continuous play of the US cine was necessary here to identify the BTX-A region. DS and 2-D-DIC resolved the injectate region at first injection frames ($t = 13$ s), but exhibited poorer delineation with increasing cine time due to tissue movement and loss of signal coherence. At $t = 15$ s, DS artifacts (CNR = 0.9) at the hyperechogenic bone region (B) were removed by 2-D-DIC, but at $t = 60$ s, additional fascia (F) and bone artifacts (B) could only be partially compensated, and the injection region was challenging to visualize (CNR = 1.2).

Spatiotemporal Filtering successfully removed most background tissue artifacts, allowing delineation of the BTX-A region over time (CNR = 2.5). In this case, no acoustic shadowing effects are visible. SE (CNR = 2.6) caused a satisfactory delineation of tissue swelling strains over the injectate region, with a minor increase in bk artifacts over time. The injectate echogenicity contrast profile stabilized in 1.2 s, and the strain profile flattened after 1 s. This is a shorter time span than the 3 s in which injectate was continuously applied. Observation of the cine revealed that the injectate spread area did not grow after 1.2 s, with additionally injected BTX-A remaining confined to the same region.

Histopathological assessment of dynamics of BTX-A infiltration. For all quantitative algorithms (DS, 2-D-DIC, SF and SE), the temporal median of each video (US cine) was calculated to summarize the

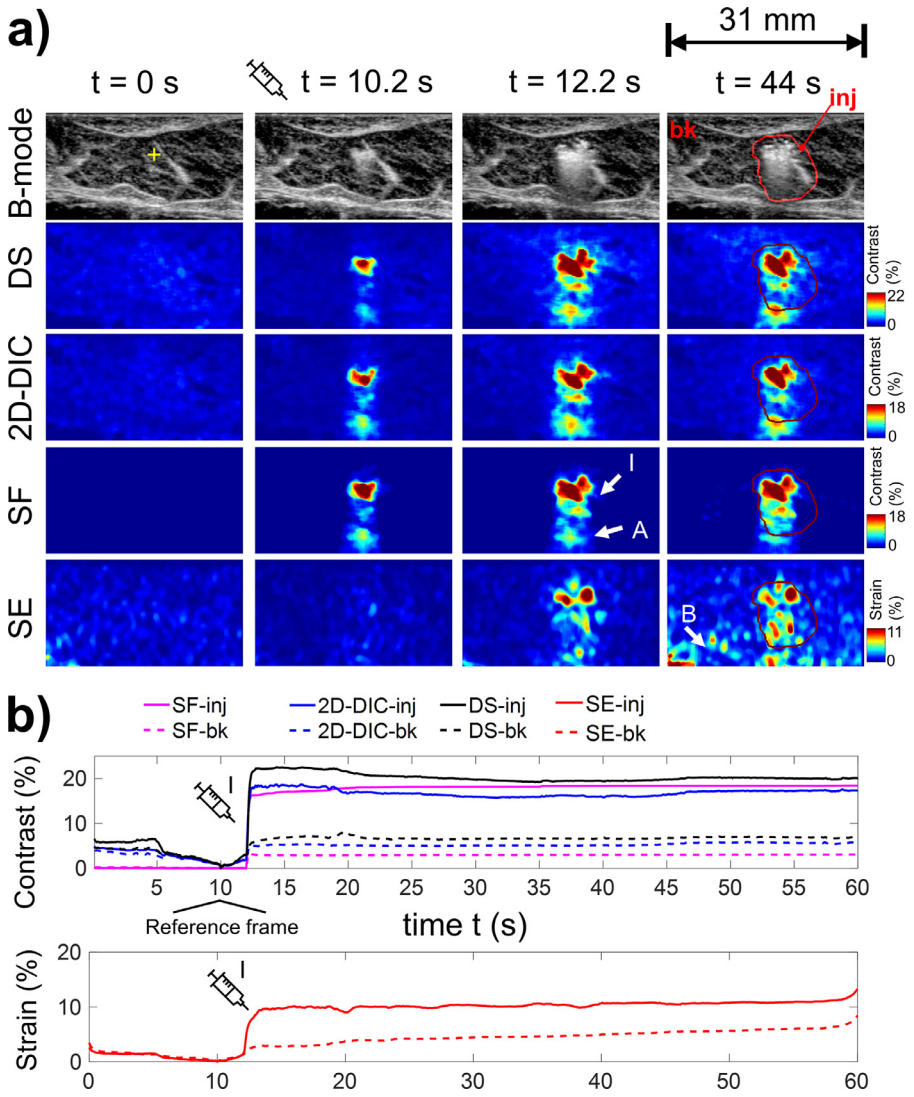

Fig. 4. Ultrasound-guided injection of NaCl with contrast agent in muscle phantom. (a) Selected injectate snapshots for B-mode and quantification algorithms of Figure 3 (direct subtraction [DS], 2-D Digital Image Correlation [2-D-DIC] and Spatiotemporal Filtering [SF]) over a cine recording time of 60 s. The color bars are adjusted to the maximum observed variations. Needle tip is marked with a *yellow cross* at $t = 0$ s. Injection starts at 10.2 s and is marked with a syringe symbol. At $t = 44$ s, cine annotation of injectate spread region (inj) is plotted as a red contour. Injectate (I), acoustic shadows (A) and artifacts in bone (B) are visible. (b) Time profiles of echogenicity contrast (DS, 2-D-DIC, SF) and swelling strain (SE) over injection annotation (inj) and background (bk) regions. Injection start is marked with a syringe symbol. SF reduces background noise with respect to DS, 2-D-DIC and SE, while preserving injectate delineation.

injection process into a single frame, which was then compared with manual US and histopathological annotations. In Figure 6,visualizations of the histopathological BTX-A spread are projected to the US coordinate system. The annotated needle tip position from the US cine images is also visualized. Defining four quadrants with respect to the needle tip (top left T-L, top right T-R, bottom left B-L and bottom right B-R), BTX-A infiltration in multiple quadrants was simultaneously observed for each sample. BTX-A infiltration in T-L was observed in 9 of 12 samples, with 8 of 12 samples for T-R, 6 of 12 samples for B-L and 2 of 12 samples for B-R. For the 8 of 12 masseter samples administered 0.25 mL injectate, the BTX-A infiltration area was 25 mm^2 (15−43 mm^2), while for the 4 of 12 masseter samples administered 0.5 mL injectate, the BTX-A infiltration area was 108 mm^2 (range: 33−222 mm^2), with a significant difference in spread between the two doses ($p = 0.013$). Longitudinal propagation of BTX-A along muscle fascia was

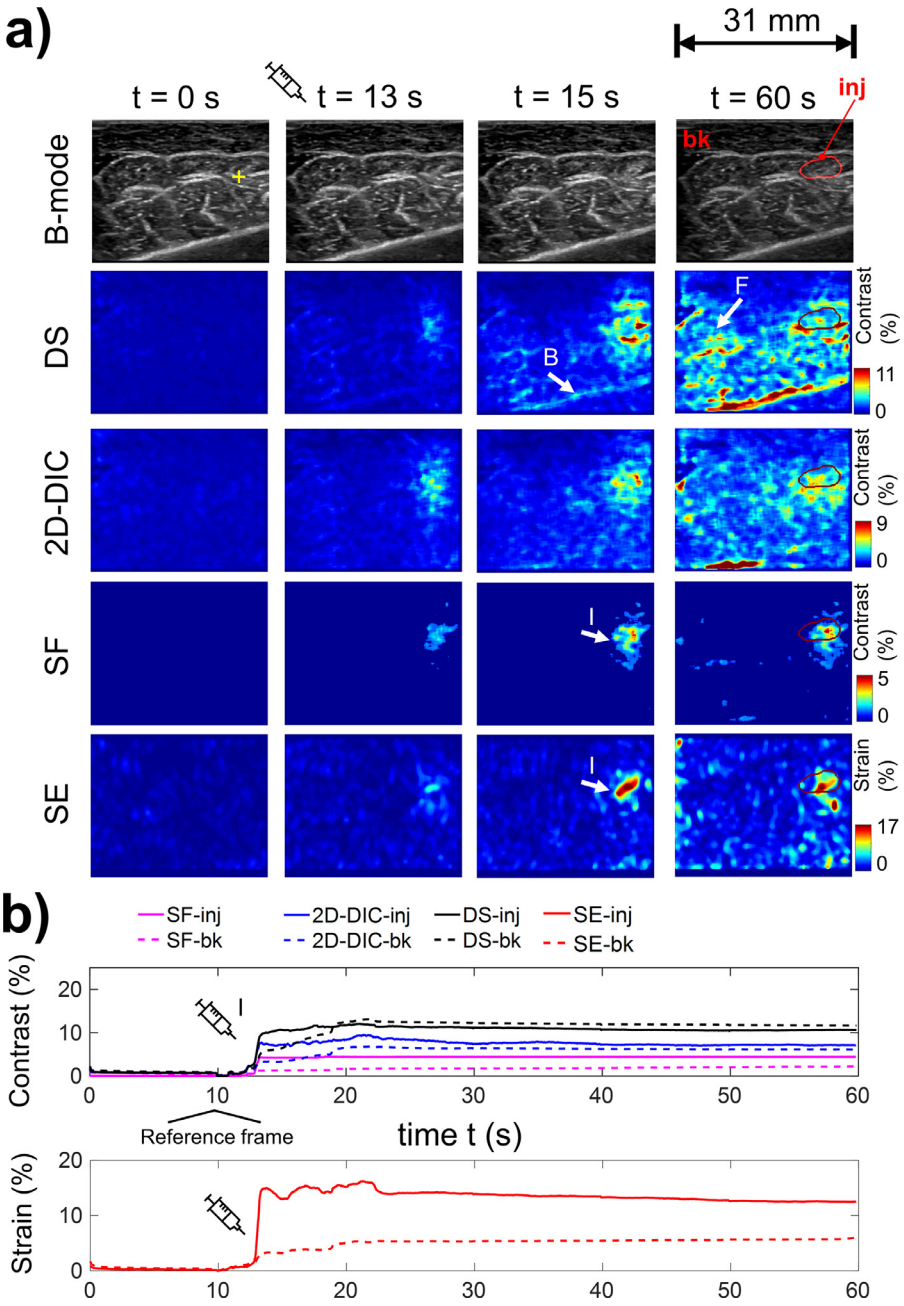

Fig. 5. Ultrasound-guided injection of BTX-A *without* contrast agent in *ex vivo* masseter M2-L. Figure legend is analogous to that of Figure 4, showing both time snapshots (a) and time profiles (b) of echogenicity contrast/strain in the injectate region (inj) with respect to background (bk). Injection occurs at $t = 13$ s, and injectate spread reaches its end position around $t = 15$ s. Because of tissue movement, the direct subtraction (DS) algorithm exhibits artifacts around bone (B) and fascia (F), which mask the injectate region and grow more severe with increasing cine recording time ($t = 60$ s). The proposed strain elastography (SE) and spatiotemporal filtering (SF) algorithms filter out these artifacts, allowing for a clear delineation of the injectate region (I), with minor differences between $t = 15$ s and $t = 60$ s.

observed, which seemed to build a border for distribution, particularly in cases M3-R and M6-L. Furthermore, a backward distribution of BTX-A into the stitch channel could be seen, when the syringe was pulled out, particularly in M1-R.

Manual ultrasound annotation. Over the N = 12 measured *ex vivo* masseter samples, the US readers evaluated the effort required for the two-frame annotation (first and last B-mode frames) with Likert between 2 and 4 and median value 3 (neutral), while cine-based

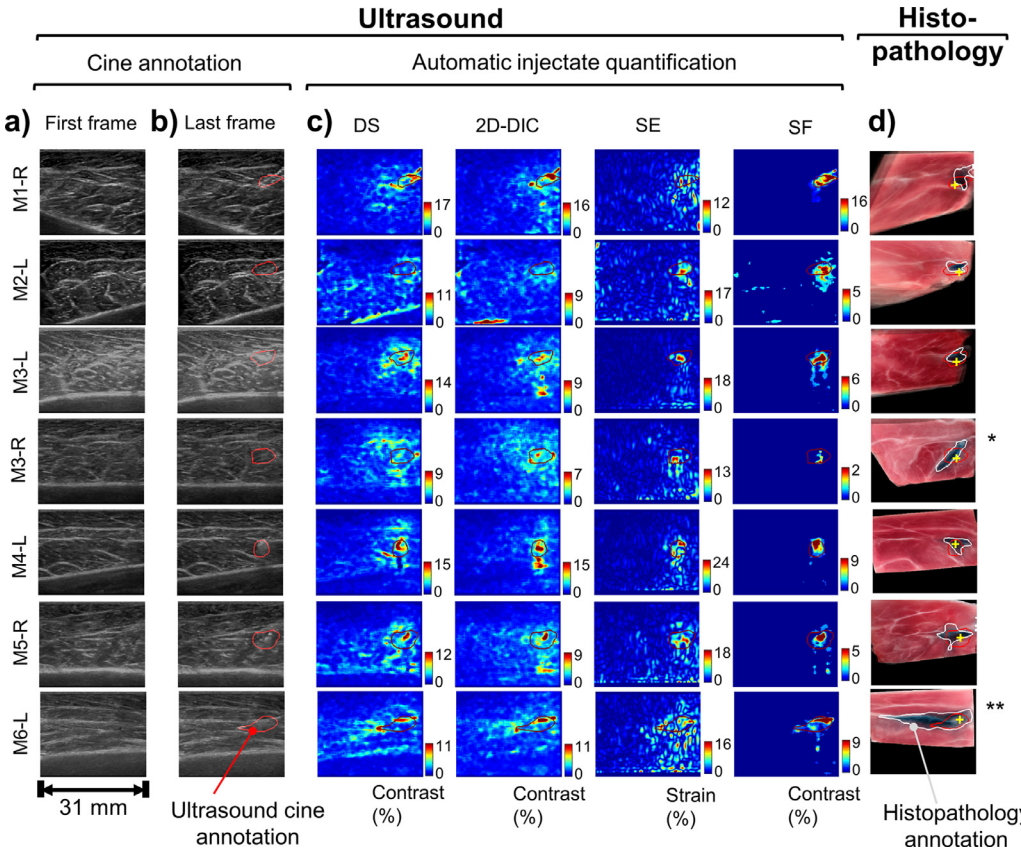

Fig. 6. Injectate spread in exemplary porcine masseter MX-R/L (X (1−6): subject index, L = left masseter, R = right masseter) after 50 s of injection. Ultrasound (US) images (a) before and (b) 50 s after BTX-A injection. (c) For each injection, the four automatic BTX-A injectate spread quantification algorithms (Fig. 3) are compared. (d) Histopathology (HP) images co-registered with US images. The consensus US cine annotation is plotted as a *red contour* in (b)−(d). The HP annotation is plotted as a *white contour* in (d). Needle tip positions in (d) are marked with a *yellow cross*. The color bars are adjusted to the maximum observed variations.

annotation was evaluated with Likert between 1 and 4 and median value 2 (easy).

The Dice coefficient between two reader BTX-A annotations was 0.64 for two-frame annotation and 0.76 for cine annotation (Fig. 7), with no significant differences between the two ($p = 0.144$). Inter-reader error in BTX-A spread surface estimation was 16.2 mm^2 (CI = 8−21 mm^2) for two-frame annotation and 10.7 mm^2 (CI = 6−16 mm^2) for cine annotation, with no significant difference ($p = 0.14$). Inter-reader error in needle tip position based on cine annotation was 0.42 mm (CI: 0.1−0.7 mm).

Comparison between histopathology and ultrasound annotation. Visual comparison (Fig. 6) of US cine annotations (*red solid line*) with histopathological annotations (*white solid line*) revealed a good spread delineation agreement for 7 of 12 cases (for instance, M1-R, M2-L, M3-L, M4-L, M5-R). In 1 of 12 cases (not shown), there was sliding displacement caused by wrong scalpel fixation, and tissue was excised outside the US region of interest. In 4 of 12 cases (for instance, M3-R, M6-L) BTX-A propagated further to the muscle fibers on histopathology than on US. Among these 4 of 12 cases, in 2 of 12 cases (for instance, M6-L) the additional spread not captured by the US probe is associated with the inhomogeneity of the BTX-A distribution in the transducer elevation plane (Fig. 8c). For the remaining 2 of 12 cases (for instance M3-R) no elevational inhomogeneity of BTX-A distribution is observed (Fig. 8b).

Registration position uncertainty between US and histopathology based on the method illustrated in Figure 2c was 1.0 mm. On comparison of US and histopathology BTX-A spread annotations, Dice was 0.43 for two-frame annotation and 0.48 for full cine annotation, with no significant differences ($p = 0.104$). BTX-A spread surface estimation uncertainty was significantly larger ($p = 0.007$) for US two-frame annotation (10.9 mm^2, CI = 0−22 mm^2) than for US full cine annotation (7.6 mm^2, CI = 4−11 mm^2). There were no statistically

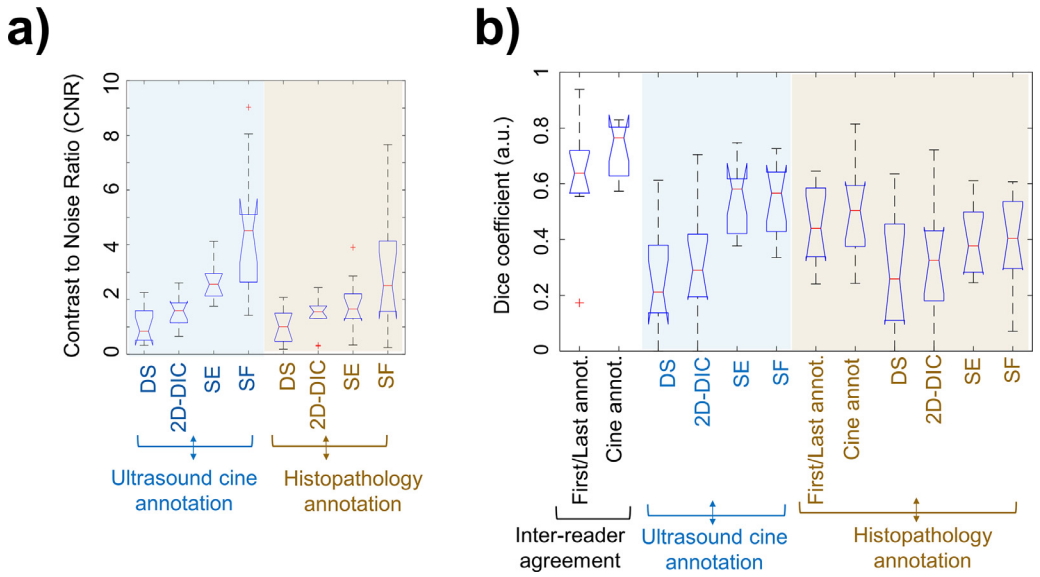

Fig. 7. (a) Contrast-to-noise ratio (CNR) and (b) Dice coefficient for automatic ultrasound injectate spread quantification algorithms: Direct Subtraction (DS), 2-D Digital Image Correlation (2-D-DIC), Strain Elastography (SE), and Spatio-temporal Filtering (SF). CNR and Dice metrics are calculated with respect to both ultrasound cine and histopathology annotations. The Dice coefficient is also calculated for inter-reader annotation agreement (first/last frame annotation and annotation of ultrasound cine). On each box, the central line indicates the median, and the bottom and top edges indicate the 25th and 75th percentiles, respectively. The whiskers extend to the 99% percentiles for normally distributed data; outliers are plotted with a plus symbol. The notches of the box provide the 95% confidence interval for the median.

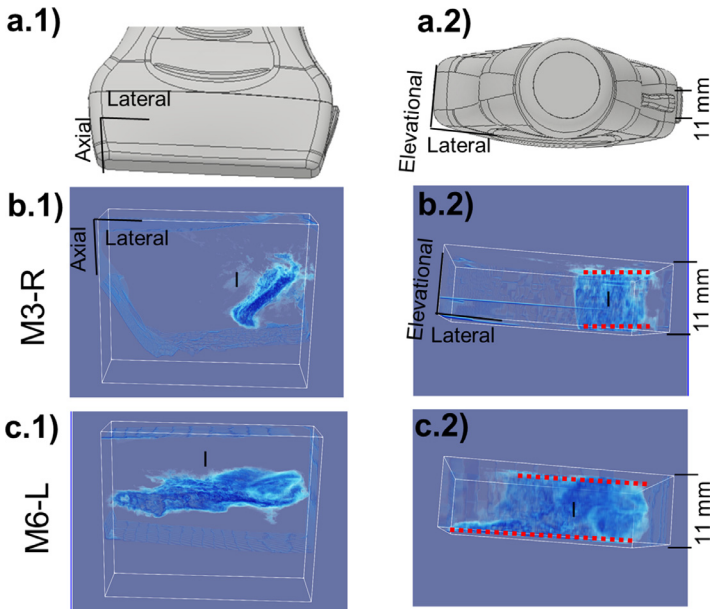

Fig. 8. Three-dimensional visualization of botulinum toxin type A (BTX-A) injectate distribution over ultrasound (US) measurement region. (a) Two-dimensional US probe used in the experiments. Two-dimensional US images are generated in the axial-lateral plane (a.1). The out-of-plane resolution (a.2) is finite, with a slice thickness of 11 mm limited by the elevation aperture of the US probe. (b, c) Histopathology (HP) volumes for two masseter samples (M3-R and M6-L in Fig. 6), where (b.1) and (c.1) illustrate the BTX-A distribution in the axial−lateral plane, and (b.2) and (c.2), the BTX-A distribution along the US probe elevation. M3-R exhibits a constant BTX-A distribution over US slice thickness (*dashed red lines* of same length in b.2), which leads to a good agreement between US and HP injectate delineation in Figure 6. M6-L exhibits a strongly varying BTX-A distribution over US slice thickness (*dashed red lines* of different length in (c.2), which leads to an US underestimation of injectate extension with respect to HP in Figure 6.

significant differences between optic and US area spread for either two-frame annotation ($p = 0.308$) or cine annotation ($p = 0.245$).

Comparison between automatic injectate quantification algorithms. In Figure 6, two US injection process representations are summarized for seven porcine masseter muscles: the temporal median of detected echogenicity (DS, 2D-DIC, SF) and the temporal median of strain variations over the 50-s injection process (SE). Confirming the observations of Figure 5, the SF algorithm exhibited superior noise rejection in background tissue regions compared with DS and 2-D-DIC, effectively filtering out artifacts at hyper-echogenic tissue structures (muscle fascia, bone interfaces). Acoustic shadowing by the BTX-A injectate increased echogenicity in the axial region below the injectate, which was observed in M3-L, M5-R and M6-L, with a less pronounced effect than in the experiments with contrast agent in Figure 4. SE effectively measured an increase in tissue swelling at the annotated injectate region for all 12 of 12 porcine masseter samples. Visually, SE exhibited superior noise rejection compared with DS and 2-D-DIC. The mean echogenic contrast variation over the annotation mask after the injection was 6.5% (SD = 5.0%). The swelling strain was 13.89% (SD = 3.7%).

Figure 7 illustrates CNR and Dice metrics for DS, 2-D-DIC, SE and SF, including quantiles for each metric and 95% CIs for the median. With respect to the consensus US cine annotation, the CNR of SF (4.63) was significantly higher than that of DS (1.29, $p < 0.001$), 2-D-DIC (1.81, $p < 0.001$) and SE (2.56, $p = 0.01$), while SE had a significantly larger CNR than 2-D-DIC ($p < 0.001$) and DS ($p < 0.001$). The Dice coefficient of SF (0.57) was significantly higher than those of DS (0.21, $p = 0.001$) and 2-D-DIC (0.29, $p = 0.001$), but not significantly different from that of SE (0.58, $p = 0.966$), while SE had a significantly higher Dice coefficient than DS ($p < 0.001$) and 2-D-DIC ($p = 0.002$). The inter-reader Dice coefficient between US cine annotations was significantly higher than those of SF, SE, 2-D-DIC and DS ($p < 0.001$). The inter-reader Dice coefficient between US two-frame annotations did not significantly differ from those of SF ($p = 0.064$) and SE ($p = 0.085$), but was significantly higher than those of 2-D-DIC ($p = 0.002$) and SE ($p = 0.001$). The inter-reader differences between manual annotation of needle tip position, compared to automatic needle tip detection, were not significant for SF (0.89 mm, $p = 0.341$, CI = 0.3–1.4 mm), SE (1.59 mm, $p = 0.067$, CI = 0.9–2.3 mm), 2-D-DIC (1.24 mm, $p = 0.095$, CI = 0.7–1.8 mm), and DS (1.18 mm, $p = 0.109$, CI = 0.7–1.7 mm).

With respect to histopathology annotation, the CNR of SF (2.65) was significantly higher than those of DS (1.42, $p = 0.005$), 2-D-DIC (1.76, $p = 0.014$) and SE (1.91, $p = 0.028$), while SE had a significantly larger CNR than DS ($p = 0.002$), but a not significantly larger CNR than 2-D-DIC ($p = 0.06$) (Fig. 7). With respect to histopathology annotation, manual US cine annotation revealed significantly higher Dice coefficients than automatic annotations with SF ($p = 0.0294$), SE ($p = 0.002$), 2-D-DIC ($p = 0.049$) and DS ($p = 0.019$). Manual US two-frame annotation had a significantly higher Dice coefficient than SE

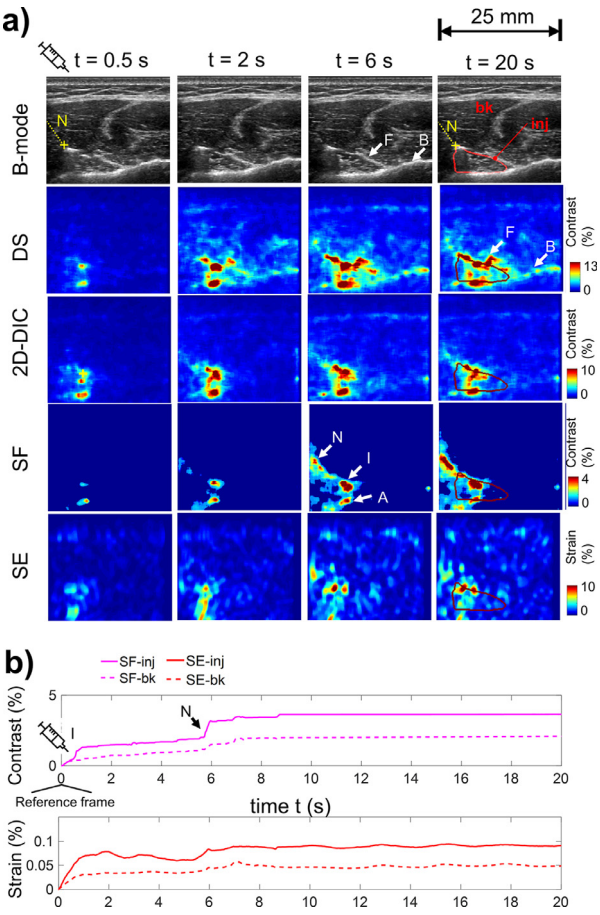

Fig. 9. Exemplary *in vivo* ultrasound-guided BTX-A injection *without* contrast agent for a patient diagnosed with idiopathic masticatory myalgia (IMM). (a) Selected injectate snapshots. The color bars are adjusted to the maximum observed variations. (b) Time profiles of echogenicity contrast and strain. Injection started at $t = 0.5$ s, with needle N marked in B-mode. At $t = 20$ s, cine annotation of injectate spread (inj) is plotted as a *red contour*. Injectate (I) is successfully delineated by the US quantification algorithms, with additional artifacts caused by tissue movement (needle N, fascia F, bone B) and acoustic shadows (A). The 2-D Digital Image Correlation (2-D-DIC), Strain Elastography (SE), and Spatiotemporal Filtering (SF) algorithms reduce bone and fascia artifacts in Direct Subtraction (DS). Acoustic shadows are alleviated by both SE and SF. Needle ejection at 6 s leads to a coherent contrast change, which is captured by SF. Otherwise, SF achieves almost total noise cancellation in the background (bk) region outside of the injectate.

($p = 0.0294$) and DS ($p = 0.043$), but did not have a significantly different Dice coefficient than automatic annotation with SF ($p = 0.1378$) and 2-D-DIC ($p = 0.106$). No statistically significant differences in BTX-A spread area were found between histopathological annotation and SE ($p = 0.2921$, Shapiro–Wilk $p = 0.016$) or SF (0.6257) segmentations.

All above-evaluated 45 *t*-test variables qualitatively approximated straight lines in a normal probability plot (not shown). Unless explicitly noted, the Shapiro–Wilk null hypothesis that the tested variable came from a normal distribution could not be rejected at a significance level $p = 0.05$ for 44 of 45 tests.

In vivo *patient*

In Figure 9, *in vivo* time snapshots of the progression of the BTX-A injectate into the patient's masseter are shown for B-mode; DS, 2D-DIC, and SF (echogenicity); and SE (strain swelling). The BTX-A injection starts at $t = 0.5$ s and progresses until 5 s, when the BTX-A spread stabilizes. With respect to the previously discussed phantom (Fig. 4) and *ex vivo* cases (Fig.5 and Fig. 6), there was significant tissue movement during the injection process. As in previous cases, DS and 2-D-DIC caused artifacts all over the US image. Both SF and SE algorithms successfully filtered out these artifacts and removed false-positive areas outside the annotated muscle injection compartment (marked as "inj" in Fig. 9a). The injection needle was extracted at $t = 6$ s, and the insertion canal (N) could be visualized through the change in echogenicity contrast. The BTX-A injectate spread was visible in B-mode and SF as a hypo-echogenic fluid region with 10% contrast (I). BTX-A spread occurred mainly in the right-bottom quadrant with respect to the needle tip. Tissue swelling strains up to 30% also could be visualized in this region. The readers consistently annotated a BTX-A injectate region larger than the one resolved by the automatic algorithms. The reason was observation of upward displacements in the fascia F, which were visually associated with BTX-A diffusion below the fascia F. However, SE did not identify tissue-swelling strains in this region. An alternative hypothesis is that the needle movement introduced displacement in the tissue structures.

DISCUSSION

B-mode US successfully visualized BTX-A injectate spread during the first seconds of the injection process. Using US contrast agent, injectate visualization by eye was possible based on single US frames (>20% contrast). However, acoustic shadowing artifacts were present because of the scattering and attenuation of US waves with the contrast agents, which complicated the delineation of injectate extent in the axial direction, in agreement with (Soetanto and Chan 2000). Without contrast agent, BTX-A injectate exhibited smaller contrast (on average 6.5%). Delineation of spread region was only possible by observation of two or more frames of US cine, where differential echogenicity variations and tissue swelling displacements (on average 13.9%) in BTX-A spread region allowed estimation of its extent. This assessment is, however, sonographer dependent, with measurable differences in annotated spread surfaces between two readers. Observation of the full cine improved the consistency of estimation of BTX-A extent area with respect to histopathology; however, the geometric delineation (Dice coefficient) of the BTX-A region did not significantly improve, and the annotation difficulty was more demanding for the readers (Likert score).

Image processing algorithms, which post-process US images to quantify tissue echogenicity contrast and tissue swelling strains caused by injectate spread, can contribute to facilitate and objectivize injection processes. Blood flow quantification in human tissues is a state-of-the-art technology based on Doppler imaging sequences, which measure the velocity of moving blood particles (Hoskins et al. 2010). For smaller vessels and lower flow velocities, such as tumor microvasculature, spatiotemporal image filters have been previously proposed to discriminate tissue movement from angiogenesis (Demené et al. 2015). Image registration before Doppler imaging also has been recently applied to decrease the rank of tissue movements and highlight microvasculature (Nayak et al. 2019). All these methods require custom ultrafast data acquisition sequences (at 1000 s frames/s) to track flow. A B-flow modality has also been proposed for flow imaging based on conventional US imaging sequences (<100 Hz frames/s) and special source coding, where image subtraction highlights moving particles with respect to the stationary background (Weskott 2000). SE can track tissue displacements as a response to mechanical excitation, which allows discrimination between stiff and soft tissues (Shiina et al. 2015). Template matching is regularly used in SE to measure tissue deformation and strain (Huang et al. 2019). SE has also been found to detect temperature variations in tissues (Souchon et al. 2005) or swelling strains associated with the progression of a thermal ablation front (Baki et al. 2015). Automatic visualization of injectate spread in soft tissues has so far received considerably less attention. Image registration with respect to a reference frame has been reported to improve the visualization of contrast agents (Gardner et al. 2004; Dave and Forsberg 2009; Hansen et al. 2016) or to improve the assessment of tissue echogenicity variations caused by pathologic processes (Seo et al. 2005). These works rely on DS or deformation compensation (2-D-

DIC) of individual frames with respect to a reference frame.

In this work, we analyzed the temporal dynamics of the BTX-A injection processes and built up algorithms that exploit their spatiotemporal characteristics to measure tissue echogenicity changes (SF) and swelling strains (SE). The benefits of SF are visually clear in Figures 4, 5, 6 and 9, where no deformation compensation (DS) and deformation compensation without SF (2-D-DIC) are compared with SF in different scenarios, including use or no use of contrast agent, and both *ex vivo* and *in vivo* cases.

With our current setup, BTX-A injectate spread built up an average surface of 50 mm^2 in <3 s, which corresponds to a flow velocity of <0.15 cm/s. This is two orders of magnitude below the range of operation of Doppler systems, which typically display velocities of tens of centimeters per second (Oglat et al. 2018). On the other hand, B-mode frame rates (here 25 frames/s) were enough to acquire multiple observations (25−75) of the injectate spread process. It was observed that DS imaging of injection spread in muscles was limited by misalignment of echogenic tissue structures (for instance, muscle fascia and bone interfaces), which led to artifactual brightness patterns that masked the visualization of injectate spread. 2-D-DIC was found to significantly reduce these artifacts with respect to DS, yet it is limited by deformation bias of template matching toward echogenic patterns. 2-D-DIC also suffers from loss of tracking coherence and decorrelation with the initial reference frame with increasing cine time. The effect was observed in Figure 4 as an increase in background noise a few seconds after the injection start, and it is probably owing to out-of-plane tissue displacements during the injection process, which were not accounted for by the 2-D template matching. SF successfully differentiated dynamic injectate echogenicity patterns from stationary tissue deformation bias, and effectively filtered out background noise, thereby significantly increasing CNR with respect to DS and 2-D-DIC. By operating on differential displacements and echogenicity images, decorrelation with increasing cine time could be avoided. Strain elastography (SE) discriminated injectate presence in terms of local tissue swelling, with CNR superior to DS and 2-D-DIC, but CNR inferior to SF. The latter is probably owing to the double temporal filtering of SF in both tissue displacement and echogenicity domains (Fig. 3c), while SE only filters out noise in the displacement domain (Fig. 3d). In terms of injectate region delineation (Dice coefficient), both SE and SF were superior to 2-D-DIC and DS, but the differences between SE and SF were not significant. The disagreement of both SE delineation and SF delineation with respect to consensus two-frame annotation was not larger than inter-reader variability. Since inter-reader variability provides a measure of how accurate a consensus two-frame annotation could be defined, we can conclude that SE and SF achieves a similar performance with respect to two-frame annotation. With respect to histopathology ground truth, SF was non-inferior to manual two-frame annotation and marginally inferior to cine annotation. No over- or underestimation bias of histopathological BTX-A spread surface was found for either SE or SF. Therefore, both SF and SE shows potential as fast and objective injectate spread quantification procedures, without needing to sacrifice performance with respect to manual annotations.

Histopathology exhibited good agreement with US annotation in 8 of 12 *ex vivo* masseter cases, with small positional deviations associated with the sample preparation process. One limitation was that fascia may change its direction in the 3-D volume defined by the insonification plane and the transducer elevation and, thus, BTX-A propagation as well. In 2 of 12 cases (Fig. 8c), BTX-A exhibited an inhomogeneous distribution over the elevation axis of the transducer, which did not allow consistent monitoring of BTX-A injectate spread based on a 2-D image. For another 2 of 12 cases (Fig. 8b), a larger spread of BTX-A was observed in histopathology, which was not visible in the first seconds monitored by US. This is probably owing to a later infiltration of the injectate into the muscle fascia during sample extraction (<15 min) and start of the deep-freezing process (<60 min). Technically, the main limitation of the automatic algorithms is the limited speckle texture information available in the B-mode images, which are calculated after US demodulation and require large correlation templates (here 2×2 mm^2) for displacement tracking. Radiofrequency US data, which contain both phase and amplitude information, may potentially improve tissue displacement estimation and provide access to visualization of smaller echogenicity contrast variations (Tavakoli et al. 2010). Real-time three-dimensional ultrasound imaging may be applied to captured inhomogenous three-dimensional injectate spread distributions.

There is level 1 evidence that instrumented guidance is superior to injections relying on manual guidance for deeper muscles (Heinen et al. 2006; Alter et al. 2012; Albanese et al. 2015), where US was highlighted for precise and painless identification of target muscles with readily available equipment. Recently, simulation platforms have been developed to train sonographers in BTX-A muscle injection and infiltration (Moreno et al. 2019). So far, US guidance has been primarily used to identify the muscle areas that need to be punctured and to correctly position the injection needle. For instance, US guidance can avoid mis-injections at

the salivary gland and prevent inflammation and trauma. It can also help in deciding the adequate needle length for each patient to reach the target muscles based on the thickness of subcutaneous tissue, thereby preventing BTX-A loss and ensuring more effective therapy (Quezada-Gaon et al. 2016).

Speed injection and needle gauge are known factors that influence uptake of BTX-A (Kinnet 2004). In our experiments, a large variety of injectate spread surfaces and directions for the same injectate administration, needle gauge and injection speed were observed. Muscle was consistently identified as border structures for BTX-A distribution, building separate muscle compartments where BTX-A was confined (Fig. 6). Also, in Figure 4, the BTX-A spread occurred over the first 1.2 s of injection, with the additional 1.8 s of administration remaining confined to the same compartment. US guidance could potentially contribute to ensure a homogeneous distribution of BTX-A over the target masseter structures. As fascia connectivity occurs in three dimensions, direct observation of injectate is necessary to reveal separate spread compartments in the masseter.

One limitation of our study was the utilization of *ex vivo* porcine muscle. While porcine muscle is a suitable animal model for experimental studies (Tuxen and Kirkeby 1990), postmortem decomposition and rigor mortis influence muscle structure. Moreover, no biological reactions or cardiovascular system is present to process BTX-A. Further *in vivo* studies are necessary to investigate the influence of blood flow in drug distribution. The viscosity of indigo carmine, which was used to dye the histopathological samples, may also impair the distribution of BTX-A. The proposed experimental setup is designed to illustrate that ultrasound imaging offers adequate visualization of the injectate distribution, which is objectively consistent with histopathology. Preliminary results revealed that the proposed automatic injectate segmentation algorithms were applicable to *in vivo* scenarios. Both SF and SE algorithms effectively filtered out tissue movement (*e.g.,* needle and patient movement) and artifacts outside the target muscle compartments and revealed echogenicity contrast variations and swelling strains in the BTX-A spread regions. For the *in vivo* case described (Fig. 9), the two readers consistently identified a larger BTX-A spread region than the automatic algorithms, based on observed tissue displacements. However, the tissue displacements outside the BTX-A region were not associated with tissue swelling in SE images. A larger population should be studied to parametrize and differentiate tissue displacements caused by BTX-A infiltration from needle and physiologic patient movement.

Apart from BTX-A infiltration monitoring, the proposed method may be advantageous for other clinical applications, such as US guidance in regional anesthesia (Marhofer et al. 2005; McCartney et al. 2010; Andersen et al. 2012; Sasaki et al. 2017). Visual qualitative US guidance has been applied to monitor spread of local anesthetic, which allowed real-time identification of misdistributions of the anesthetic solution and guaranteed a faster onset time than the control groups. Also the anesthetic dose can be injected as close as possible to the nerve, thus lowering the dose and reducing costs and toxicity risks. By minimizing the number of required injections, potential complications can be reduced, for instance, pneumothorax or pleural puncture during rip fractures or breast surgery, where the anesthetic solution is injected into the paravertebral space (Marhofer et al. 1998; Willschke et al. 2006; Santonastaso et al. 2018).

CONCLUSIONS

US B-mode allowed monitoring of BTX-A injectate spread during the first minute of the injection process, in agreement with histopathological observations. Spatio-temporal filtering algorithms and SE can quantify echogenic contrast differences and tissue swelling during the deformation process and provide objectivization with respect to visual assessment. US allows identification of bounded BTX-A spread compartments within the muscle tissue limited by muscle fascia.

Acknowledgments—This research has been financially supported by the Swiss National Science Foundation under SNF Project 156466, “Advanced Magnetic Resonance Imaging for Diagnosis and Therapy in Patients with Temporomandibular Joint (TMJ) Disorders." This project has been generously supported by a donation from Dr. Hans-Peter Wild to the University Hospital Zurich Foundation.

Conflict of interest disclosure—The authors declare there are no conflicts of interest.

APPENDIX

Co-registration of histopathological images into three-dimensional stack

The plugin "Register Virtual Stack Slices" uses the Scale Invariant Feature Transform (SIFT) (Lowe 2004) for automatic robust feature identification. Outliers are filtered out using the Random Sample Consensus (RANSAC) (Fischler and Bolles 1981). The registration of the images is performed with a free affine transformation model for the full optic image and then fine-tuned with a second registration over the tissue region of interest. Figure 2 b.2 shows a 3-D render of the BTX-A region of the registered stack, which was generated with ParaView software (Ahrens et al. 2005).

Implementation of algorithm building blocks

US frames were pre-processed to eliminate headers, normalized to a scale 0 to 1, cropped to the HP region of interest, and binned by a factor of 2 to an isotropic pixel size (axial, lateral) of 100 μm x 100 μm (Fig. 2 a).

Deformation tracking DT^{ij} between B-mode frames F_a, F_b was performed with two-dimensional zero-normalized cross-correlation (ZNCC) (Pan et al. 2009) to estimate the axial $u(i, j)$ and v(i, j) lateral displacements fields for each axial i and lateral j image pixels (Eq A1):

$$\mathbf{u}_{b,a} = [u(i,j), v(i,j)] = \operatorname{argmax}_{l,m \in [-S,S]} r_{F_a,F_b}(l,m)$$

$$r_{F_a,F_b}(l,m) \frac{\sum_{w_j=-W_J}^{W_J}\sum_{w_i=-W_I}^{W_I}\left[F_b(i+l+w_i,j+l+w_j)-\bar{F}_b\right]\left[F_a(i+w_i,j+w_j)-\bar{F}_a\right]}{\sum_{w_j=-W_J}^{W_J}\sum_{w_i=-W_I}^{W_I}\left[F_b(i+l+w_i,j+l+w_j)-\bar{F}_b\right]^2 \sum_{w_j=-W_J}^{W_J}\sum_{w_i=-W_I}^{W_I}\left[F_a(i+l+w_i,j+l+w_j)-\bar{F}_a\right]^2} \quad \text{(A1)}$$

where $\bar{F}_b$ and $\bar{F}_a$ are average values respect the summation ranges. A template matching block $W_I \times W_J$ of 20 × 20 pixels (2 mm × 2 mm), together with a search space S of 10 pixels (1 mm) were used. For 2-D sub-pixel estimation of deformation fields, a 6-coefficient non-separable two-dimensional parabola was fitted with least squares to the maximum of the ZNCC function and its 9 neighboring lags [-1, 0, 1], following the method of (Azar et al. 2010).

The interpolation block I^{ij} was implemented with bilinear interpolation, using the 9 neighboring lags [-1, 0, 1] of each pixel to estimate sub-pixel gray-scale values. The high-pass filter $HPF_n(F_n^{i,j}) = F_n^{i,j} - MF_n(F_n^{i,j}, N)$ is based on a one-dimensional median filter MF_n along the temporal axis n. The filter order N was 100 (4 s) for differential displacements ($HPF1_n$) and 30 (1.2 s) for differential contrast images ($HPF2_n$). The spatial filter step was implemented with a two-dimensional median filter MF^{ij} of order 3 (0.3 mm), followed by a threshold cut for contrast values <0.02. All final SE, 2-D-DIC and SF images were presented in the plots in absolute contrast units, and additionally filtered with a two-dimensional median filter of order 10 (1 mm) to facilitate visualization and automatic segmentation.

Strain fields were calculated with a weighted least-squares estimator based on (Kallel and Ophir 1997) (Eq A2):

$$\varepsilon_u(i,j) = \frac{\sum_{k\in\mathbf{K}}\sum_{l\in\mathbf{L}}\hat{u}(i+k,j+l)\sum_{j\in\mathbf{J}}\sum_{i\in\mathbf{I}} i(i+k,j+l) - S_\lambda \sum_{k\in\mathbf{K}}\sum_{l\in\mathbf{L}} i(i+k,j+l)\hat{u}(i+k,j+l)}{\left[\sum_{k\in\mathbf{K}}\sum_{k\in\mathbf{K}}\hat{i}(i+k,j+l)\right]^2 - S_\lambda \sum_{k\in\mathbf{K}}\sum_{k\in\mathbf{L}} w_{k,l} i(i+k,j+l)^2}$$

$$\varepsilon_v(i,j) = \frac{\sum_{k\in\mathbf{K}}\sum_{l\in\mathbf{L}}\hat{v}(i+k,j+l)\sum_{j\in\mathbf{J}}\sum_{i\in\mathbf{I}}\hat{j}(i+k,j+l) - S_\lambda \sum_{k\in\mathbf{K}}\sum_{l\in\mathbf{L}} j(i+k,j+l)\hat{v}(i+k,j+l)}{\left[\sum_{k\in\mathbf{K}}\sum_{k\in\mathbf{K}}\hat{j}(i+k,j+l)\right]^2 - S_\lambda \sum_{k\in\mathbf{K}}\sum_{k\in\mathbf{L}} \lambda_{k,l} j(i+k,j+l)^2} \quad \text{(A2)}$$

$$\hat{u} = u_{k,l}\lambda_{k,l}\hat{v} = v_{k,l}\lambda_{k,l}\hat{i} = i_{k,l}\lambda_{k,l}\hat{j} = j_{k,l}\lambda_{k,l} S_\lambda = \sum_{k\in\mathbf{K}}\sum_{l\in\mathbf{L}} j\lambda_{k,l}$$

$$\mathbf{K} = [-W_I, W_I] \quad \mathbf{L} = [-W_J, W_J]$$

where the window $W_I \times W_J$ of 20 × 20 pixels (2 mm × 2 mm) defines the strain resolution. $\lambda_{k,l}$ is a weighted smoothing kernel, implemented with a two-dimensional Hanning window.

Figure A1 shows an example of the calculation of Strain Elastography (SE) images for *ex vivo* masseter (M2-L). B-mode images are provided as a reference (Fig. A1 a). Exemplary tracked axial deformation $\Delta\mathbf{u}$ (Fig. A1 b) and temporally filtered differential displacements $\tilde{\Delta}\mathbf{u}$ (Fig. A1 c) are shown, corresponding to the outputs of steps Figure 3 c1 and Figure 3 c2. The temporal filtering step filters out deformation bias at hyperechogenic muscle fascia, which are visible as quasi-horizontal displacement patterns in $\Delta\mathbf{u}$, thus highlighting the deformation at the injectate region in Figure A1 c. Figure A1 d and A1 e show the cumulative deformation fields corresponding to the output of Figure 3 c3, which are used as input to the SE calculation process (Fig. 3 d).

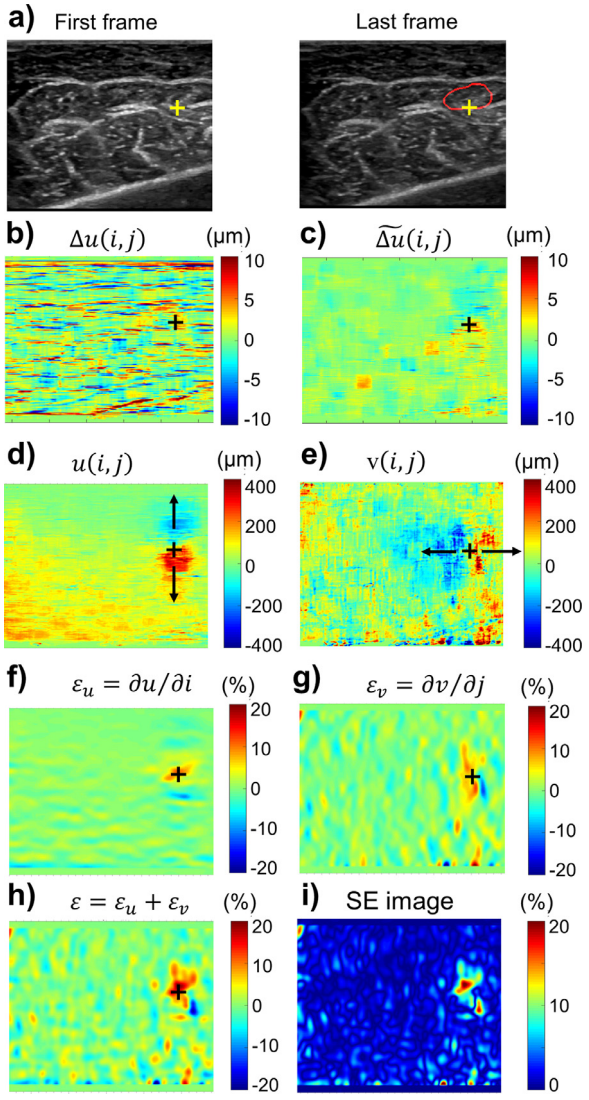

Figure A1. Detailed steps of Strain Elastography (SE) image calculation, illustrated exemplarily for ex-vivo masseter M2-L. a) As a visual reference, B-mode images of the injection process and US cine annotation are shown. The needle tip position is marked with a cross. Differential displacements are shown before Δu (b) and after $\tilde{\Delta}$u (c) temporal filtering, illustrating deformation bias reduction. d) Cumulative axial deformation $u(i, j)$ for each axial i and lateral j pixel of the image. e) Cumulative lateral deformation $v(i, j)$. d) Axial strain $\varepsilon_u = \partial u/\partial i$. e) Lateral strain $\varepsilon_v = \partial v/\partial j$. f) Swelling strain $\varepsilon = \varepsilon_u + \varepsilon_v$. Tissue expansion ($\varepsilon < 0$) is observed in injectate region, accompanied by compression ($\varepsilon < 0$) of adjacent tissues. i) SE images are plotted in absolute strain values $|\varepsilon|$.

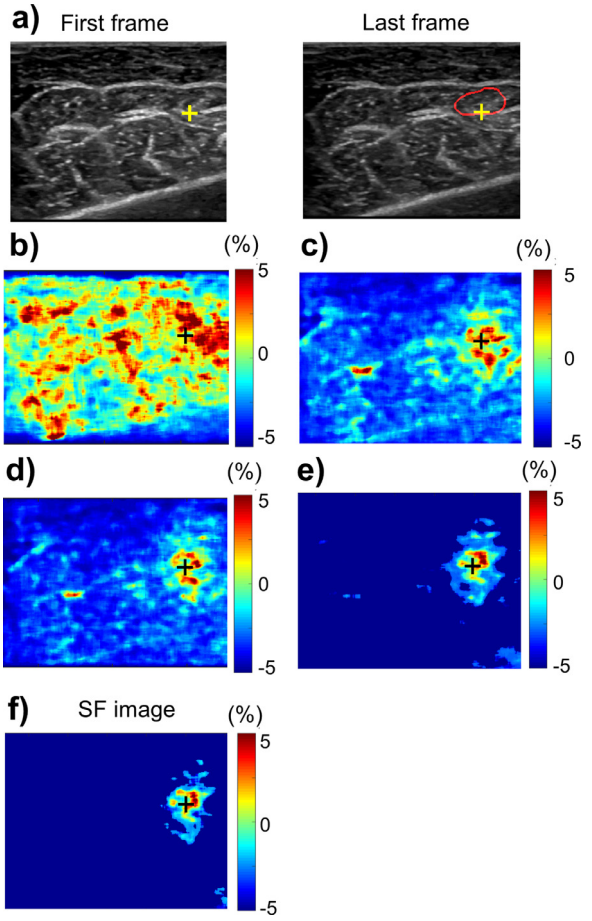

Figure A2. Detailed steps of Spatiotemporal Filtering (SF) image calculation, illustrated exemplarily for ex-vivo masseter M2-L. a) As a visual reference, B-mode images of the injection process and US cine annotation are shown. b) Intermediate SF images with none of the filters in Fig. 3c, that is, $HPF1_n$, $HPF2_n$ and MF^{ij}, activated. c) Intermediate SF images with only the temporal filter $HPF1_n$ activated. d) Intermediate SF images as in c) with temporal filter $HPF2_n$ additionally activated. e) Intermediate SF imagesas in d) with spatial MF^{ij} thresholding operation additionally activated. f) Final SF image as in e) with spatial MF^{ij} median filter additionally activated.

Tissue expansion starts at the needle tip. Therefore, deformation is in opposite polarity across the needle location. This can be observed for axial displacement (Fig. A1 d), where tissue deforms upward toward the probe ($u < 0$) above the needle tip, and downward toward the tissue ($u > 0$) below the needle tip. Similarly, for lateral displacement (Fig. A1 e): on the right of the needle tip, tissue deforms from left most pixel to right most pixel ($v > 0$). On the left side of the needle tip, tissue deforms from right most pixel to left most pixel ($v < 0$). As outlined in Figure 3 d, tissue swelling ε is calculated by adding up axial gradients of displacement (ε_u, Fig. A1 f) and lateral gradients of displacement (ε_v, Fig. A1 g). Tissue shows expansion ($\varepsilon > 0$) in the direction of injectate propagation, accompanied by tissue compression ($\varepsilon < 0$) in adjacent tissues to accommodate injectate-induced deformation (Fig.A1 h). Since tissue expansion and compression showed heterogeneous patterns for different samples, it was overall observed that

using absolute strains |ε| (Fig. A1 i) was adequate to evaluate the extent of injectate presence.

Figure A2 exemplifies the calculation of echogenicity contrast images with Spatiotemporal Filtering (SF) for M2-L, thereby highlighting the impact of the filters in the final images. B-mode images are provided as a reference (Fig. A2 a). Figure A2 b shows the SF calculation, when the temporal filtering of the differential displacements ($HPF1_n$, Fig. 3 c.2) is suppressed. Due to the accumulation of bias deformation components in each differential step, the resulting SF image shows reduced contrast between background and injectate. Figure A2 c shows the SF image with $HPF1_n$ active but we no further filtering of echogenicity frames. The injectate region is successfully revealed. Figure A2 d shows the SF image after temporal filtering $HPF2_n$ in Figure 3 c.7, noise outside the injectate region is further reduced. The contribution is small in this example, since the probe setup is fixed and no physiologic movement is present. Figure A2 e shows the SF image after thresholding the differential echogenicity frames in Figure 3 c.8 before accumulation. The threshold filter separates noise and dynamic injectate components in the gray-scale histogram, contributing to the delineation of the injection region. Figure A2 f shows the additional noise reduction effect of the spatial median filter MF^{ij} in Figure 3.c8, providing the final SF image.

REFERENCES

Ahrens J, Geveci B, Law C. ParaView: An end-user tool for large data visualization. In: Hansen CD, Johnson CR, (eds). Visualization handbook. : Elsevier; 2005. p. 717–731.

Albanese A, Abbruzzese G, Dressler D, Duzynski W, Khakova S, Marti MM, Mir P, Montecucco C, Moro E, Pinter M. Practical guidance for CD management involving treatment of botulinum toxin: A consensus statement. J Neurol 2015;262:2201–2213.

Alter KE, Karp BI. Ultrasound guidance for botulinum neurotoxin chemodenervation procedures. Toxins (Basel) 2018;10:E18.

Alter KK, Nichols S, Skurow SM. Chemodenervation: Ultrasound characteristics of relevant tissues. In: Alter KK, Hallet M, Karp BI, (eds). Ultrasound guided chemodenervation procedures: Text and atlas. New York: Demos Medical; 2012. p. 124–137.

Andersen HL, Andersen SL, Tranun-Jensen J. Injection inside the paraneural sheath of the sciatic nerve direct comparison among ultrasound imaging, macroscopic anatomy, and histologic analysis. Reg Anesth Pain Med 2012;37:410–414.

Arganda-Carreras I, Sorzano COS, Marabini R, Carazo JM, Ortiz-De-Solorzano C, Kybic J. Consistent and elastic registration of histological sections using vector-spline regularization. In: Beichel RR, Sonka M, (eds). Computer vision approaches to medical image analysis. CVAMIA 2006. Lecture Notes in Computer Science 2006;4241. Berlin/Heidelberg: Springer; 2006.

Awan KH. The therapeutic usage of botulinum toxin (Botox) in non-cosmetic head and neck conditions—An evidence based review. Saudi Pharm J 2017;25:18–24.

Azar RZ, Goksel O, Salcudean S. Sub-sample displacement estimation from digitized ultrasound RF signals using multi-dimensional polynomial fitting of the cross-correlation function. IEEE Trans Ultrason Ferroelectr Freq Control 2010;57:2403–2420.

Baki P, Sanabria SJ, Kosa G, Szekely G, Goksel O. Thermal expansion imaging for monitoring lesion depth using M-mode ultrasound during cardiac RF ablation: In vitro study. Int J Comput Assist Radiol Surg 2015;10:681–693.

Bloc S, Garnier T, Komly B, Asfazadourian H, Leclerc P, Mercadal L, Morel B, Dhonneur G. Spread of injectate associated with radial or median nerve-type motor response during infraclavicular brachial-plexus block: An ultrasound evaluation. Reg Anesth Pain Med 2007;32:130–135.

Bruyn GAW, Schmidt SW. How to perform ultrasound-guided injections. Best Pract Res Clin Rheumatol 2009;23:269–279.

Clark GT. Classification, causation and treatment of masticatory myogenous pain and dysfunction. Maxillofac Surg Clin North Am 2008;20:145–157.

Daniels EW, Cole D, Jacobs B, Phillips SF. Existing evidence on ultrasound-guided injections in sports medicine. Orthop J Sport Med 2018;6 2325967118756576.

Dave JK, Forsberg F. Novel automated motion compensation technique for producing cumulative maximum intensity subharmonic images. Ultrasound Med Biol 2009;35:1555–1563.

Demené C, Deffieux T, Pernot M, Osmanski BF, Biran V, Gennisson JL, Sieu LA, Bergel A, Franqui S, Correas JM, Cohen I, Baud O, Tanter M. Spatiotemporal clutter filtering of ultrafast ultrasound data highly increases Doppler and fultrasound sensitivity. IEEE Trans Med Imaging 2015;34:2271–2285.

Dogu O, Apaydin D, Sevim S, Talas DU, Aral M. Ultrasound-guided versus "blind" intraparotid injections of botulinum toxin-A for the treatment of sialorrhoea in patients with Parkinson's disease. Clin Neurol Neurosurg 2004;106:93–96.

Epis O, Bruschi E. Interventional ultrasound: A critical overview on ultrasound-guided injections and biopsies. Clin Exp Rheumatol 2014;32:S78–S84.

Figgit D, Noble S. Botulinum toxin B: A review of its therapeutic potential in the management of cervical dystonia. Drugs 2002;62:705–722.

Fischler MA, Bolles RC. Random sample consensus: A paradigm for model fitting with applications to image analysis and automated cartography. Commun ACM 1981;24:381–395.

Gardner EA, Sumanaweera TS, Steins R, Woelmer MN, Leen E. Removing local motion from ultrasonic images using nonaffine registration for contrast quantification. Proc IEEE Int Ultrason Symp 2004;1718–1721.

Guarda-Nardini L, Manfredini D, Salamone M, Salmaso L, Tonello S, Ferronato G. Efficacy of botulinum toxin in treating myofascial pain in bruxers: A controlled placebo pilot study. Cranio 2008;26:126–135.

Hansen KB, Villagomez-Hoyos CA, Brasen JC, Diamantis K, Sboros V, Sorensen CM, Jensen JA. Robust microbubble tracking for super resolution imaging in ultrasound. Proc IEEE Int Ultrason Symp 2016;1051–1117.

Heinen F, Molenaers G, Fairhurst C, Carr LJ, Desloovere K, Chaleat VE, Morel E, Papavassiliou AS, Tedroff K, Pascual-Pascual SI. European Consensus Table 2006 on botulinum toxin for children with cerebral palsy. Eur J Paediatr Neurol 2006;10:215–225.

Hong JS, Sathe GG, Niyonkuru C, Munin MC. Elimination of dysphagia using ultrasound guidance for botulinum toxin injections in cervical dystonia. Muscle Nerve 2012;46:535–539.

Hoskins PR, Martin K, Thrush A. Diagnostic ultrasound: Physics and equipment. 2nd ed. Cambridge, UK: Cambridge University Press; 2010.

Huang L, Korhonen RK, Turunen MJ, Finnilä MAJ. Experimental mechanical strain measurement of tissues. PeerJ 2019;7:e6545.

Kallel F, Ophir J. A least-squares strain estimator for elastography. Ultrason Imaging 1997;19:195–208.

Kinnet D. Botulinum toxin A injections in children: Technique and dosing issues. Am J Phys Med Rehabil 2004;83:S59–S64.

Kurtoglu C, Gur OH, Kurkcu M, Sertdemir Y, Guler-Uysal F, Uysal H. Effect of botulinum toxin-A in myofascial pain patients with or without functional disc displacement. J Oral Maxilofac Surg 2008;66:1644–1651.

Lowe DG. Distinctive image features from scale-invariant keypoints. Int J Comput Vis 2004;60:91–110.

Marhofer P, Schrogendorfer K, Wallner T, Koinig T, Koinig H, Mayer N, Kaparl S. Ultrasonographic guidance reduces the amount of local anesthetic for 3-in-1 blocks. Reg Anesth Pain Med 1998;23:584–588.
Marhofer P, Greher M, Kapral S. Ultrasound guidance in regional anaesthesia. Br J Anaesth 2005;94:7–17.
McCartney CJ, Dickinson V, Dubrowski A, Riazi S, McHardy P, Awad IT. Ultrasound provides a reliable test of local anesthesic spread. Reg Anesth Pain Med 2010;35:361–363.
Moreno V, Curto B, Garcia-Esteban JA, Serrano FJ, Alonso Hernandez P, Hernander Zaballos F, Juanes JA. Software suite training tool for MSK exploration and botulinumtoxin infiltration based on ultrasound imaging for the spasticity treatment. J Med Syst 2019;43:238.
Nayak R, Kumar V, Webb J, Fatemi M, Alizad A. Non-invasive small vessel imaging of human thyroid using motion-corrected spatiotemporal clutter filtering. Ultrasound Med Biol 2019;45:1010–1018.
O'Donnel M, Skovoroda AR, Shapo BM, Emelianov SY. Internal displacement and strain imaging using ultrasonic speckle tracking. IEEE Trans Ultrason Ferroelectr Freq Control 1994;41:314–325.
Oglat AA, Matjafri MZ, Suardi N, Oqlat MA, Abdelrahman MA, Oqlat AA. A review of medical Doppler ultrasonography of blood flow in general and specially in common carotid artery. J Med Ultrasound 2018;26:3–13.
Otsu N. A threshold selection method from gray-level histograms. IEEE Trans Sys Man Cyber 1979;9:62–66.
Pan B, Qian KM, Xie HM, Asundi A. Two-dimensional digital image correlation for in-plane displacement and strain measurement: A review. Meas Sci Technol 2009a;20 062001.
Quezada-Gaon N, Wortsman X, Penaloza O, Carrasco JE. Comparison of clinical marking and ultrasound-guided injection of Botulinum type A toxin into the masseter muscles for treating bruxism and its cosmetic effects. J Cosmet Dermatol 2016;15:238–244.
Razali N, Wah YB. Power comparisons of Shapiro−Wilk, Kolmogorov−Smirnov, Lilliefors and Anderson−Darling tests. J Stat Model Anal 2011;2:21–33.
Santonastaso DP, DeChiara A, Rispoli M, Musetti G, Agnoletti V. Real-time view of anesthetic solution spread during an ultrasound-guided thoracic paravertebral block. Tumori 2018;104:NP50–NP52.
Sasaki H, Yamauchi M, Ninomiya T, Tatsumi H, Yamakage M. Possible utility of contrast-enhanced ultrasonography for detecting spread of local anesthetic in nerve block. J Anesth 2017;31:365–373.
Schindelin J, Arganda-Carreras I, Frise E, Kaynig V, Longair M, Pietzsch T, Preibisch S, Rueden C, Saalfeld S, Schmid B, Tinevez JY, White DJ, Hartenstein V, Eliceiri K, Tomancak P, Cardon A. Fiji: An open-source platform for biological-image analysis. Nat Methods 2012;9:676–682.
Sconfienza L, Lacelli F, Bruno A, Serafini G. Ultrasound guidance can improve the outcome of botulinum toxin A injection. Eur J Phys Rehabil Med 2009;45:153.
Seo J, Tran BC, Hall TL, Fowlkes JB, Abrams GD, O'Donnel M, Cain CA. Evaluation of ultrasound tissue damage based on changes in image echogenicity in canine kidney. IEEE Trans Ultrason Ferroelectr Freq Control 2005;52:1111–1120.
Shiina T, Nightingale KR, Palmeri ML, Hall TJ, Bamber JC, Barr RG, Castera L, Choi BI, Chou YH, Cosgrove D, Dietrich CF, Ding H, Amy D, Farrokh A, Ferraioli G, Filici C, Friedrich-Rust M, Nakashima K, Schafer F, Sporea I, Suzuki S, Wilson S, Kudo M. WFUMB guidelines and recommendations for clinical use of ultrasound elastography: Part 1. Basic principles and terminology. Ultrasound Med Biol 2015;41:1126–1147.
Soetanto K, Chan M. Fundamental studies on contrast images from different-sized microbubbles: Analytical and experimental studies. Ultrasound Med Biol 2000;26:81–91.
Solberg WK. Temporomandibular disorders: Masticatory myalgia and its management. Br Dent J 1986;160:351–356.
Souchon R, Bouchoux G, Macjejkko E, Lafon C, Cathignol D, Betrand M, Chapelon JY. Monitoring the formation of thermal lesions with heat-induced echo-strain imaging: A feasibility study. Ultrasound Med Biol 2005;31:251–259.
Tavakoli V, Kemp J, Dawn B, Stoddard M, Amini AA. Comparison of myocardial motion estimation methods based on simulated echocardiographic B-mode and RF data. In: Molthen RC, Weaver JB, (eds). Medical imaging 2010: Biomedical Applications in Molecular, Structural, and Functional Imaging. San Diego, CA, USA: SPIE Proc; 2010. 76260N.
Tran TMN, Ivanusic JJ, Hebbard P, Barrington MJ. Determination of spread of injectate after ultrasound-guided transversus abdominis plane block: A cadaveric study. Br J Anaesth 2009;102:123–127.
Tuxen A, Kirkeby S. An animal model for human masseter muscle: Histochemical characterization of mouse, rat, rabbit, cat, dog, pig, and cow masseter muscle. J Oral Maxillofac Surg 1990;48:1063–1067.
Varghese T, Ophir J. An analysis of elastographic contrast-to-noise ratio. Ultrasound Med Biol 1998;24:915–924.
von Lindern J, Niederhagen B, Berge S, Appel T. Type A botulinum toxin in the treatment of chronic facial pain associated with masticatory hyperactivity. J Oral Maxilofac Surg 2003;61:774–778.
Weskott HP. B-flow−A new method for detecting blow flow. Ultraschall Med 2000;21:59–65.
Wieckiewicz M, Zietek M, Smardz J, Zenczak-Wieckiewicz D, Grychowska N. Mental status as a common factor for masticatory muscle pain: A systematic review. Front Psychol 2017;8:646.
Willschke H, Boesenberg A, Marhofer P, Johnston S, Kettner S, Eicheberger U, Wanzel O, Kapral S. Ultrasonographic-guided ilioinguinal/iliohypogastric nerve block in pediatric anesthesia: What is the optimal volume?. Anesth Analg 2006;102:1680–1684.
Zhou JY, Wang D. An update on botulinum toxin A injections of trigger points for myofascial pain. Curr Pain Headache Rep 2014;18:386.